Data-Driven Modeling of Wireless Power Transfer Systems With Multiple Transmitters

Fengwei Chen, Peter C. Young, Hugues Garnier, Qijun Deng, and Marian K. Kazimierczuk, *Fellow, IEEE*

***Abstract*—This article develops a new method of data-driven modeling for a class of multiple-transmitter single-receiver wireless power transfer (WPT) systems. A continuous-time multiple-input single-output (MISO) model with pure time delays is used to characterize the input–output behavior of the system, where the transfer functions associated with each input channel are not constrained to have the same denominator. Moreover, the time delays are allowed to be a fraction of the sampling interval in order to account for the delay effects that stem from circuit components and wireless communication, which are, by nature, often a fraction of the sampling interval. An optimal refined instrumental variable method is proposed to estimate the parameters and time delays of the MISO model based on sampled input–output data. In contrast to the conventional circuit-theory-based modeling methods that rely on circuit parameters and result in models which are often complex, the proposed data-based method yields parsimonious models, whose parameters are directly estimated from input–output data. Due to the easy availability of sampled data in control engineering applications, the proposed method is clearly more user-friendly, having a broad prospect for efficient operation of WPT systems, such as prediction, optimization, and control. Numerical and experimental results are presented to validate the effectiveness and merit of the proposed method.**

***Index Terms*—Data-driven modeling, instrumental variable (IV) method, multiple-input single-output (MISO) system, time-delay estimation, wireless power transfer (WPT).**

Manuscript received September 26, 2019; revised February 19, 2020; accepted April 18, 2020. Date of publication April 19, 2020; date of current version July 20, 2020. This work was supported in part by the National Natural Science Foundation of China under Grants 61703311, 51677139, 51977151, and 61903057, in part by the China Postdoctoral Science Foundation under Grant 2017M620335, and in part by the Shenzhen Science and Technology Innovation Committee under Grant JCYJ2017081811280674. Recommended for publication by Associate Editor F. W. Fuchs. *(Corresponding authors: Fengwei Chen; Qijun Deng.)*

Fengwei Chen is with the School of Electrical Engineering and Automation, Wuhan University, Wuhan 430072, China (e-mail: fengwei.chen@whu.edu.cn).

Peter C. Young is with the Systems and Control Group, Lancaster Environment Centre, Lancaster University, Lancaster LA1 4YQ, U.K. (e-mail: p.young@lancaster.ac.uk).

Hugues Garnier is with the Centre de Recherche en Automatique de Nancy, Centre National de la Recherche Scientifique, Université de Lorraine, F-54000 Nancy, France (e-mail: hugues.garnier@univ-lorraine.fr).

Qijun Deng is with the School of Electrical Engineering and Automation, Wuhan University, Wuhan 430072, China, and also with the Shenzhen Research Institute, Wuhan University, Shenzhen 518057, China (e-mail: dqj@whu.edu.cn).

Marian K. Kazimierczuk is with the Department of Electrical Engineering, Wright State University, Dayton, OH 45435 USA (e-mail: marian.kazimierczuk@wright.edu).

Color versions of one or more of the figures in this article are available online at https://ieeexplore.ieee.org.

Digital Object Identifier 10.1109/TPEL.2020.2989155

I. Introduction

WIRELESS power transfer (WPT) based on magnetic resonant coupling has been recognized as a preferred technology for mid-range power delivery [1], [2]. WPT is beneficial for scenarios, where power cable connections are inconvenient or not allowed, with applications ranging from portable devices [3], wireless sensors [4], and biomedical implants [5], [6] to electric vehicles [7]–[9]. The power transfer efficiency of WPT systems is known to be very sensitive to the magnetic coupling link between the transmitter and receiver coils, which is strongly dependent on factors such as coil geometry, placement, and ambient interference. In view of this background, there are a few papers in which multiple or arrayed transmitters are employed to power a single receiver in order to improve the range, reliability, and gain of power transfer. These show that multiple-input single-output (MISO) WPT systems generally outperform their single-input single-output (SISO) counterparts in terms of overall power transfer efficiency [10]–[15]. At the same time, however, use of multiple transmitters brings new challenges for analysis, design, and optimization of WPT systems, due to the increase in the number of degrees of freedom [13].

Over the past few years, considerable efforts have been made to address the aforementioned problems. In [10], an upper bound of power transfer efficiency in the near-field WPT under the multiple-transmitter scenario was established. In [11], the effect of coupling between transmitters and receivers was investigated, and some guidelines were suggested on how to adjust the resonant and/or driving frequencies for maximum efficiency. In [12], the coupling, gain, and diversity effects were investigated in further detail with the help of a simple circuit model, and a new power line synchronization technique was proposed to synchronize all transmitter coils to achieve maximum efficiency. More recently, a new convex optimization framework was formulated in [13] to optimize the power transfer efficiency, where the original nonconvex problem was reformulated into a convex one, so that constraints on the transmitting power could be imposed conveniently.

The aforementioned papers all concentrated on circuit-level analysis of MISO WPT systems, while system-level analysis, with particular reference to dynamic modeling in the input–output form necessary for control system design, has been considered less. To fill this gap, the focus of this article is on the control-oriented modeling of MISO WPT systems. There are already several circuit-theory-based methods available in the literature [16]–[23], and a few of them can build transfer

function or state-space models for SISO WPT systems, e.g., the first-harmonic approximation method [17], [18], the state-space averaging method [19], the coupled mode-based method [20], and the sampled-data model approach [22]. The aforementioned methods have been shown to be effective when the circuit component parameters are known *a priori* or can be experimentally measured. However, the determination of these parameters is often difficult in industrial applications due to technical or economic reasons, and consequently, good performance of conventional methods may not be guaranteed, especially when the system parameters can vary with respect to time. In addition, these methods were initially developed for SISO WPT systems, so that their generalization to the MISO scenario is not trivial because coupling also occurs among the transmitters, not only between the transmitters and receiver, making the circuit analysis very difficult. Another shortcoming of circuit-theory-based methods is the complication of the resulting models, which are of high order and not suitable for control system design unless a model reduction step has been performed [24], [25]. In this regard, it is necessary to develop an efficient and user-friendly method for fast and accurate dynamic modeling.

In contrast to circuit-theory-based modeling, data-driven modeling, referred to as "system identification" in the control literature [26]–[28], adopts a rather straightforward approach to avoid the problem of overparameterization. In particular, it uses a parsimonious, gray-, or black-box model, the order and structure of which is identified from the data, to explain the output data and then estimates the parameters that characterize this model by minimizing a quadratic cost function defined by the mean-squared errors between the predicted and measured outputs [27]. Since sampled input–output data are easier to acquire than the true circuit component parameters, the data-driven approach is more user-friendly and can always yield simple models that are very suitable for control system design. Therefore, data-driven modeling has been attracting increasing attention in the field of power electronics [29]–[32]. Moreover, as the model parameters are optimal in the mean-squared error sense and no model reduction is necessary, the data-driven approach can outperform the conventional approaches in terms of model efficiency and accuracy.

In our previous work [25], data-driven modeling of a SISO WPT system has been investigated, using a continuous-time (CT) or discrete-time (DT) transfer function, plus a time delay, to explain the input–output behavior of the system. Here, the method employed to estimate the associated model parameters and time delay is the frequency-domain version of the refined instrumental variable (RIV)-based method proposed in [33]. The merit of modeling in the frequency domain is that both CT and DT models can be estimated in a uniform manner. In this article, we generalize the method in [33] to estimate MISO time-delay models for WPT systems. The contributions of this article are twofold.

1) A parsimonious MISO model with pure time delays is proposed to explain the input–output behavior of a MISO WPT system, where *parsimonious* means that the number of parameters is as small as necessary to explain the input–output behavior of the system. Here, for parsimonious parameterization, the transfer functions associated with each transmitter are not constrained to have the same denominator, so allowing for fully independent parameterization of each input channel.
2) Robust implementation of the proposed method is investigated. The generalization of the method in [33] to estimate MISO time-delay models is more challenging than in the SISO case, due to the multimodality nature of the cost function, which becomes more severe in the presence of multiple time delays. Therefore, how to increase the chance of global convergence is a problem of great practical value.

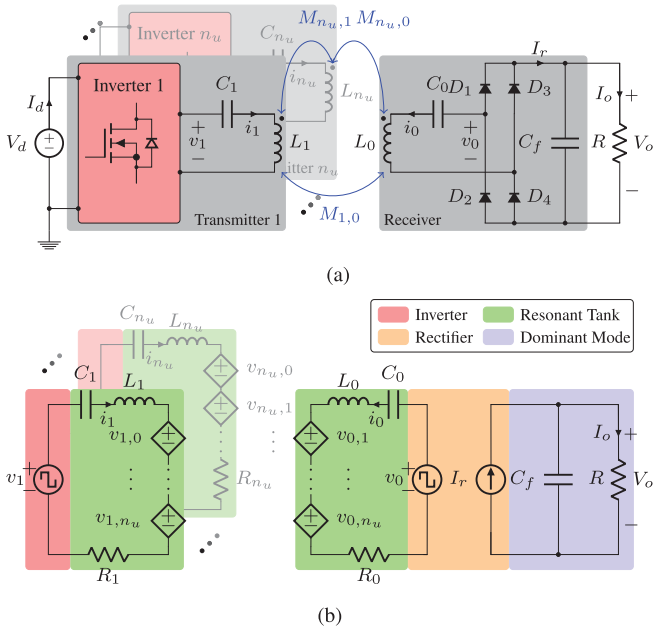

Fig. 1. MISO WPT system under consideration. In deriving the equivalent circuit, the switches and diodes are regarded as ideal components. R_j, $j = 0, 1, \ldots, n_u$, accounts for the equivalent series resistance of the jth resonator. v_j, $j = 1, \ldots, n_u$, is an ac source to replace the phase-controlled inverter of the jth transmitter. $v_{j,k}$, $j \neq k$, is the controlled voltage source to replace the mutual inductance $M_{j,k}$. (a) Circuit diagram. (b) Equivalent circuit.

The remainder of this article is organized as follows. The MISO WPT system and its model are introduced in Section II. After that, a new RIV-based method to estimate the parameters and time delays of the model is proposed in Section III. Practical considerations for efficient implementation of the proposed method are discussed in Section IV. Subsequently, simulation and experimental examples are presented in Sections V and VI that confirm the merit and effectiveness of the proposed method. Finally, Section VII concludes this article.

II. Preliminaries

A. WPT System

This article considers a series–series compensated MISO WPT system with n_u inverters, as shown diagrammatically in Fig. 1. As a convention throughout this article, each component in the system is labeled with a subscript j ($0 \leqslant j \leqslant n_u$): $j > 0$

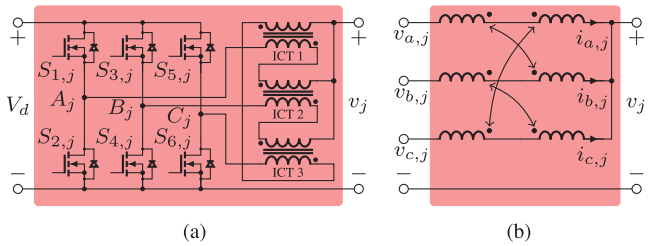

Fig. 2. Three-phase inverter. (a) Circuit diagram. (b) Equivalent circuit.

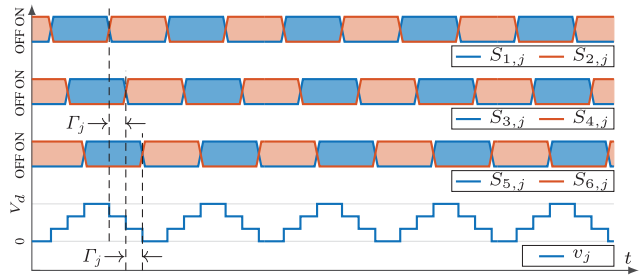

Fig. 3. Typical signal waveforms in the three-phase inverter.

means it is a component from the jth transmitter, while $j = 0$ means it is a component from the receiver. Each transmitter consists of a phase-controlled inverter, a coil L_j, and a compensating capacitor C_j, $1 \leqslant j \leqslant n_u$. The receiver consists of a coil L_0, a compensating capacitor C_0, a full-bridge rectifier, and an output filter capacitor C_f. This WPT setup assumes loose coupling between the transmitter and receiver coils, i.e., the mutual inductance $M_{j,k}, 0 \leqslant j \leqslant n_u, 0 \leqslant k \leqslant n_u, j \neq k$, is small, while the leakage inductance is large, so that the role of C_j is to compensate for the inductive behavior of L_j (see [21] and [34] for more analysis and design issues regarding loosely coupled transformers).

It is worth noting that magnetic coupling in the MISO setting not only occurs between a transmitter coil and the receiver coil, but also between any two transmitter coils. The prominent merit of series–series compensation is that the choice of compensating capacitors is independent of the load [18]. In order to allow for significant power transfer through loosely coupled coils, however, the transmitter and receiver resonators should have the same resonant frequency defined by [35]

$$\omega_0 = \frac{1}{\sqrt{L_0 C_0}} = \cdots = \frac{1}{\sqrt{L_{n_u} C_{n_u}}} \text{ rad/s} \tag{1}$$

and the driving frequencies of each inverter need to be synchronized with the same frequency and phase [12].

B. Dominant Mode Analysis

In this subsection, the analysis considers the dominant physical mechanism of the WPT system from a circuit theory stand point and investigates how this can be modeled in the simplest manner. The aim of such dominant mode analysis (see, e.g., [36]) is to derive a low-order dynamic model that is able to capture the most important dynamics of the WPT system and provide a basis for control system design. Note that the simulation results in Figs. 5 and 7 are generated from the simulated system presented in Section V. The parameters remain in their default settings unless any change in these is mentioned specifically.

1) Inverter: The inverter converts the dc source voltage to a high-frequency ac voltage in order to ensure the efficient transfer of electrical power through loosely coupled coils. Among the available circuit topologies, two will be adopted in this article: the full-bridge inverter [25] and the three-phase inverter [24], [37]. The three-phase inverter is more suitable for high-power applications, due to the use of more switches. Fig. 2 shows its circuit diagram, where three intercell transformers (ICTs) are used to suppress possible circulating currents among inverters, and Fig. 3 shows the typical signal waveforms generated in the circuit. It is assumed that all of the ICT windings are identical, i.e., the magnetizing inductances, as well as the leakage inductances, are the same.

The three-phase inverter will be considered here and in Section V. However, only the full-bridge inverter was available for experimental work, and this will be considered in Section VI. The only difference between the two types of inverter is the modulated output. The three-phase inverter gives an output described in (2), and the full-bridge inverter gives an output described by (56) in Section VI.

For the regulation of the output voltage V_o, a set of control variables, denoted as $\{\Gamma_j\}$, is often chosen as the phase between adjacent switching legs (see also [38]–[40]). According to circuit theory, if the switches are regarded as ideal components [37], the output voltage of the jth inverter has the following analytical expression:

$$\begin{aligned} v_j &= \frac{1}{3}\left(v_{a,j} + v_{b,j} + v_{c,j}\right) \\ &\approx \frac{2V_d}{3\pi}\left[\sin\left(\omega_s t - \Gamma_j\right) + \sin\left(\omega_s t\right) + \sin\left(\omega_s t + \Gamma_j\right)\right] \\ &= \frac{2V_d}{3\pi}\left[1 + 2\cos(\Gamma_j)\right] \cdot \sin(\omega_s t) \end{aligned} \tag{2}$$

where $v_{a,j}$, $v_{b,j}$, and $v_{c,j}$ are the voltages at points A_j, B_j, and C_j, respectively, in Fig. 1. Note that v_j in (2) has been approximated by its first harmonic. This is quite reasonable and will not introduce significant approximation errors. This is because the resonant tank is highly frequency selective and only the first harmonic can pass through, while the other higher order terms are blocked. From (2), it is clear that v_j reduces from the maximum to zero when Γ_j varies from 0 to $2\pi/3$ rad. Another feature of the inverter is input nonlinearity, i.e., the input Γ_j is passed through a static nonlinearity function $f(\Gamma_j)$ of the form

$$f(\Gamma_j) = 1 + 2\cos\left(\Gamma_j\right). \tag{3}$$

The above analysis indicates that the inverter is a memoryless device: it acts promptly to the change of Γ_j and does not influence the low-frequency behavior of the system.

2) Resonant Tank: The resonant tank has an equivalent circuit shown in Fig. 4, where the mutual inductances have been replaced by controlled voltage sources. As an example, a portion of the signals in a two-input resonant tank is shown in Fig. 5.

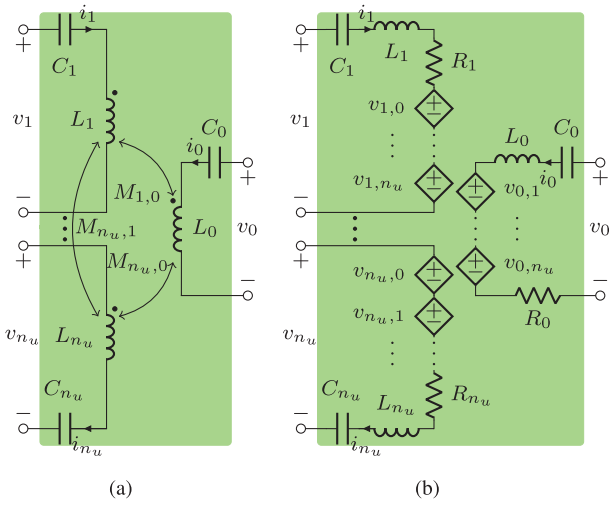

Fig. 4. Resonant tank. The controlled voltage source $v_{j,k}$ $(j \neq k)$ is defined by $v_{j,k} = M_{j,k} \cdot di_k/dt$. (a) Circuit diagram. (b) Equivalent circuit.

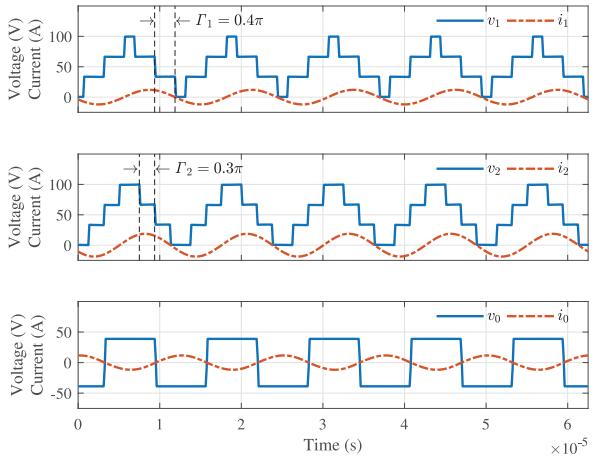

Fig. 5. Signals in a two-input resonant tank.

In total, there are $2(n_u + 1)$ reactive components in the resonant tank, so the order of the model should be $2(n_u + 1)$ according to the circuit theory. Fortunately, however, since the resonant tank is operated around the resonant frequency, at which the inductive behavior of each resonator is canceled by the capacitor connected in series, the model order can be further reduced to $(n_u + 1)$, and we obtain

$$\begin{cases} i_0(R + R_0) + \sum_{k=1}^{n_u} M_{0,k} \frac{di_k}{dt} = 0 \\ i_1 R_1 + \sum_{k=2}^{n_u} M_{1,k} \frac{di_k}{dt} = v_1 \\ \cdots \\ i_{n_u} R_{n_u} + \sum_{k=1}^{n_u - 1} M_{n_u,k} \frac{di_k}{dt} = v_{n_u} \end{cases} \tag{4}$$

where a resistive load R is assumed to the resonant tank, i.e., $v_0 = i_0 R$. Letting p denote the differential operator, i.e., $p = \frac{d}{dt}$, the above equations can be written in the more compact matrix form

$$\begin{bmatrix} R_0 + R & M_{0,1}p & \cdots & M_{0,n_u}p \\ M_{1,0}p & R_1 & \cdots & M_{1,n_u}p \\ \vdots & \vdots & \ddots & \vdots \\ M_{n_u,0}p & M_{n_u,1}p & \cdots & R_{n_u} \end{bmatrix} \begin{bmatrix} i_0 \\ i_1 \\ \vdots \\ i_{n_u} \end{bmatrix} = \begin{bmatrix} 0 \\ v_1 \\ \vdots \\ v_{n_u} \end{bmatrix}. \tag{5}$$

The output voltage of the resonant tank v_0 is then obtained as

$$v_0 = i_0 R \tag{6}$$

where i_0 is obtained from the solution of the above equation. However, the expression for v_0 can be very complicated when n_u is large, so only $n_u = 1$ and 2 are investigated in this section. In these cases, we have

$$v_0 = \begin{cases} \dfrac{M_{1,0}Rp}{M_{1,0}^2 p^2 - R_1(R_0 + R)} v_1, & n_u = 1 \\ \dfrac{B_1(p)}{A(p)} v_1 + \dfrac{B_2(p)}{A(p)} v_2, & n_u = 2 \end{cases} \tag{7}$$

where it is assumed that $M_{j,k} = M_{k,j}$ and

$$B_1(p) = M_{2,1}M_{2,0}Rp^2 - M_{1,0}R_2Rp \tag{8}$$

$$B_2(p) = M_{2,1}M_{1,0}Rp^2 - M_{2,0}R_1Rp \tag{9}$$

$$A(p) = 2M_{2,1}M_{1,0}M_{2,0}p^3 - R_1M_{2,0}^2p^2 - R_2M_{1,0}^2p^2 - (R_0 + R)M_{2,1}^2p^2 + R_1R_2(R_0 + R). \tag{10}$$

The above models reveal some properties of the resonant tank. For example, the models have at least one pole located in the right-half plane, indicating model instability. However, this instability does not affect the output v_0 because the first harmonics of the inputs v_1 and v_2 are zero mean, so that the output v_0 is also zero mean. In addition, because the WPT system is operated at the resonant mode in order to cancel the effects of L_j and C_j and so eliminate the reactive components from the equivalent circuit, it is not hard to see that the resonant tank has very fast dynamics, i.e., the modulation envelope of v_0 can track the set point quickly. For example, when $n_u = 1$, and R_0 and R_1 tend to zero, we have

$$\lim_{R_0, R_1 \to 0} v_0 = \frac{R}{M_{1,0}p} v_1 \tag{11}$$

showing that v_0 is proportional to the integral of v_1. Then, the sluggish behavior in the modulation envelope of v_0, introduced by the resonant tank, is negligible due to the very high driving frequency. A two-input case is illustrated numerically in the next subsection.

3) Rectifier and Output Filter: The rectifier recovers the modulation envelopes of the ac signals v_0 and i_0 by inverting their negative half-cycles to positive (see Figs. 6 and 7 for the circuit and signal waveforms). Obviously, this inversion does not affect the low-frequency behavior of the system, due to the absence of reactive components.

Next to the rectifier is a capacitor C_f, connected in parallel in order to smooth the output voltage. Normally, C_f should be as large as possible in order to attenuate various types of ripples and spikes in V_o. In this regard, the block of C_f and

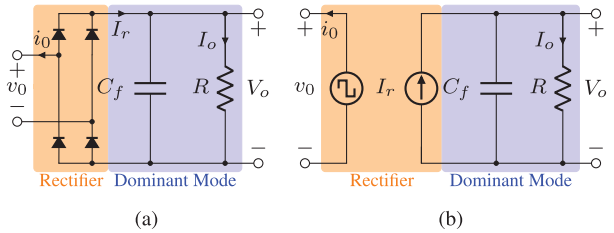

Fig. 6. Rectifier and dominant circuit. (a) Circuit diagram. (b) Equivalent circuit.

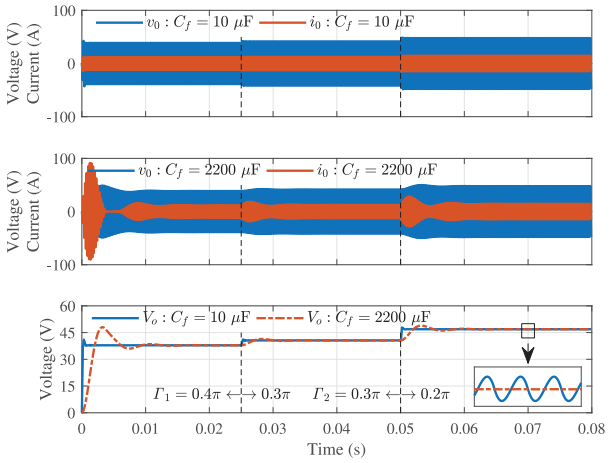

Fig. 7. Dynamical responses of a two-input WPT system under different output capacitances.

R is the only low-frequency part of the circuit and can be considered as the source of the dominant mode that characterizes the low-frequency behavior of the system. This fact is illustrated in Fig. 7, where the responses of a two-input WPT system under two different C_fs are compared. When $C_f = 10\,\mu$F, a very quick response in the amplitude of the dc output V_o (see the bottom panel of Fig. 7), as well as in the modulation envelopes of the ac signals v_0 and i_0 (see the top panel of Fig. 7), can be observed when Γ_1 steps from 0.4π to 0.3π rad, and when Γ_2 steps from 0.3π to 0.2π rad. At the same time, these results confirm our claim about the fast dynamics of the resonant tank in the previous subsection. By contrast, when a larger value $C_f = 2200\ \mu$F is used, the ripples of V_o are satisfactorily attenuated, but much slower transients appear in V_o, as well as the modulation envelopes of v_0 and i_0 (see the middle and bottom panels of Fig. 7), which validates the correctness of our dominant mode analysis.

Finally, the transfer function that relates V_o and I_r can be obtained straightforwardly, according to the circuit theory, as

$$V_o = G_o(p) I_r = \frac{1/C_f}{p + 1/(RC_f)} I_r \tag{12}$$

showing that a first-order model should be enough to capture the low-frequency behavior of the whole system, as confirmed later by the data-based analysis.

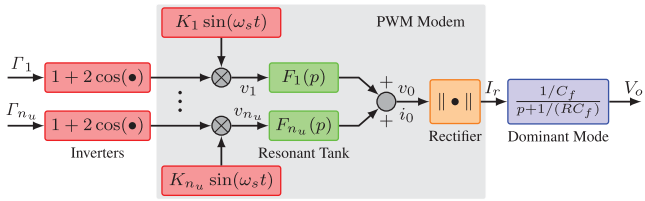

Fig. 8. Block diagram of a MISO WPT system, where $K_1, \ldots, K_{n_u}$ are constants, and $F_1(p), \ldots, F_{n_u}(p)$ are the transfer functions corresponding to each channel of the resonant tank.

C. Model Formulation

According to the analysis in the previous subsection, the WPT system can be described diagrammatically by Fig. 8. If the system is operated around the resonant state and the output capacitor C_f is very large, the high-frequency circuit (i.e., the block named "PWM modem" in Fig. 8) can be viewed as a set of static gains $K_1, \ldots, K_{n_u}$, each corresponding to an input channel. Then, the WPT system can be described by a nonlinear model of Hammerstein type [32]

$$V_o = \sum_{j=1}^{n_u} K_j G_j(p) f(\Gamma_j) \tag{13}$$

where $G_j(p)$ is the linear transfer function, and $f(\Gamma_j) = 1 + 2\cos(\Gamma_j)$ is the input nonlinearity function defined in (3). The selection of the order of $G_j(p)$ is dependent on the mode of operation: if all the resonators are operated at the resonant state exactly, the resonant tank will be resistive, and thus, $G_j(p)$ can be specified as a first-order model inspired by (12); otherwise, the resonant tank may be inductive or capacitive, so a higher order model may need to be adopted in order to capture the additional resonant tank dynamics. Further details regarding model order selection are discussed in Section IV.

Linear models are often desired for control system design, so one can linearize (13) at the given set point to obtain a small-signal model that is linear in the variables. For this purpose, let us decompose the input and output signals as

$$V_o = \overline{V}_o + v_o,\ \Gamma_j = \overline{\Gamma}_j + \gamma_j \tag{14}$$

where $\overline{V}_o$ and $\overline{\Gamma}_j$ denote the stationary values; and v_o and γ_j denote the small-signal parts. By linearizing the nonlinearity function $f(\Gamma_j)$, the small-signal version of (13) can be obtained as

$$\begin{aligned} v_o &= \sum_{j=1}^{n_u} K_j G_j(p) \frac{\partial f(\Gamma_j)}{\partial \Gamma_j}\bigg|_{\Gamma_j = \overline{\Gamma}_j} \gamma_j \\ &= -2 \sum_{j=1}^{n_u} K_j \sin\left(\overline{\Gamma}_j\right) G_j(p) \gamma_j. \end{aligned} \tag{15}$$

The main objective of this article is to derive a method for inferring small-signal models, such as the above, for WPT systems from simulated or experimental input–output data.

For clarity of notation, the input γ_j and output v_o defined in (15) are written hereafter as $u_j(t)$ and $y(t)$, respectively. As a more general version of (15), the hybrid Box–Jenkins (HBJ)

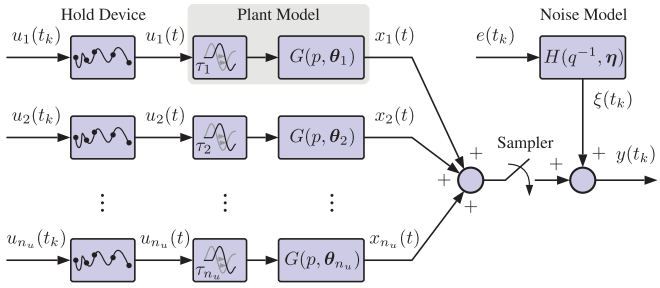

Fig. 9. Block diagram of the HBJ model with n_u inputs given in (16).

model [41], [42] with n_u inputs is used to describe the input–output behavior of the system (see also Fig. 9)

$$\begin{cases} x_j(t) = G(p,\boldsymbol{\theta}_j)u_j(t-\tau_j) = \dfrac{B(p,\boldsymbol{\theta}_j)}{A(p,\boldsymbol{\theta}_j)}u_j(t-\tau_j) \\ \xi(t_k) = H(q^{-1},\boldsymbol{\eta})e(t_k) = \dfrac{D(q^{-1},\boldsymbol{\eta})}{C(q^{-1},\boldsymbol{\eta})}e(t_k) \\ e(t_k) = \mathcal{N}(0,\sigma^2) \\ y(t_k) = \sum_{j=1}^{n_u} x_j(t_k) + \xi(t_k) \end{cases} \tag{16}$$

where, in the case of the second to fourth DT equations, the sampling interval is T; $t_k = kT$ is the sampling instant; $e(t_k)$ is a zero-mean, serially uncorrelated, and normally distributed white noise sequence of variance σ^2; and τ_j accounts for the total time lag of the jth input channel.

$G(p,\boldsymbol{\theta}_j)$ is the rational transfer function of the jth input channel, whose numerator and denominator polynomials are of the forms

$$B(p,\boldsymbol{\theta}_j) = b_{0,j}p^{m_j} + b_{1,j}p^{m_j-1} + \cdots + b_{m_j,j} \tag{17}$$

$$A(p,\boldsymbol{\theta}_j) = p^{n_j} + a_{1,j}p^{n_j-1} + \cdots + a_{n_j,j} \tag{18}$$

where p is the differentiation operator, n_j and m_j ($n_j \geqslant m_j$) are polynomial degrees, and $\boldsymbol{\theta}_j$ is a vector of the unknown rational model parameters

$$\boldsymbol{\theta}_j = \left[a_{1,j},\ldots,a_{n_j,j},b_{1,j},\ldots,b_{m_j,j}\right]^\top. \tag{19}$$

The noise model is included in the second equation of (16) in order to improve the explanatory ability of the whole model. This is because colored noise, as generated in (16) by passing the white noise source $e(t_k)$ through a DT autoregressive moving average (ARMA) filter $H(q^{-1},\boldsymbol{\eta})$, is commonly encountered in real applications. Also, it can be introduced artificially during the measurement process, e.g., using an *LCR* low-pass filter to avoid the aliasing effect. The polynomials that characterize this ARMA noise model are defined in terms of the shift operator q^{-1}, i.e., $q^{-1}\xi(t_k) = \xi(t_{k-1})$, as

$$D(q^{-1},\boldsymbol{\eta}) = 1 + d_1q^{-1} + \cdots + d_{n_d}q^{-n_d} \tag{20}$$

$$C(q^{-1},\boldsymbol{\eta}) = 1 + c_1q^{-1} + \cdots + c_{n_c}q^{-n_c} \tag{21}$$

and the unknown model parameters are gathered in vector $\boldsymbol{\eta}$

$$\boldsymbol{\eta} = [c_1,\ldots,c_{n_c},d_1,\ldots,d_{n_d}]^\top. \tag{22}$$

The word *hybrid* is applied to the model (16) because the plant is modeled in the CT domain, while the noise is modeled in the DT domain. This hybrid formulation of the model is motivated by the difficulty in estimating a CT noise model directly in a stochastic differential equation form, while the alternative ARMA noise model is much simpler to estimate and entirely adequate for most practical purposes.

The use of CT models to represent the main system dynamics is appealing for several reasons [43]–[45]. First, CT model parameters usually provide physical insights into the system and, therefore, are particularly suitable for physical modeling. Second, when the sampling interval is too small, DT models can suffer from the problem of numerical instability, but CT models do not have this problem since CT model parameters are independent of the sampling interval. Third, in estimation terms, CT models are a natural choice to handle fractional time delays because, in DT models, time delays are naturally constrained to be an integer number of sampling intervals T, due to the use of shift operators, unless the time delay is processed separately and the integer delayed input is replaced by the fractionally delayed input.

Finally, note that it is often required that the input–output signals are sampled rapidly for CT model estimation, e.g., it is best if the sampling interval T is short, so that the associated sampling frequency is about five to ten times the system bandwidth, or even larger than this if possible (see, e.g., [28, Sec. 8.7]).

D. Objective

Assume that the following conditions are considered and satisfied throughout this article.

1) The CT input $u_j(t)$ is generated from a DT sequence $\{u_j(t_k)\}_{k=1}^N$ via a known hold device. $\{u_j(t_k)\}_{j=1}^{n_u}$ are zero mean, mutually uncorrelated, and persistently exciting.
2) $G(p,\boldsymbol{\theta}_j)$ is compact, causal, and asymptotically stable. More specifically, the roots of $A(p,\boldsymbol{\theta}_j)$ are all located on the left-half plane; $B(p,\boldsymbol{\theta}_j)$ and $A(p,\boldsymbol{\theta}_j)$ do not have any common factors. Moreover, the denominators $\{A(p,\boldsymbol{\theta}_j)\}_{j=1}^{n_u}$ are not necessarily constrained to be identical.
3) $H(q^{-1},\boldsymbol{\eta})$ is stable and invertible, that is, $C(q^{-1},\boldsymbol{\eta})$ and $D(q^{-1},\boldsymbol{\eta})$ are co-prime, with all roots located within the unit circle. $e(t_k)$ is zero mean, white, and uncorrelated with the inputs.
4) The degrees $\{n_j,m_j\}_{j=1}^{n_u}$, n_c, and n_d are known.

The objective of this article is to estimate the parameter vectors $\{\boldsymbol{\theta}_j\}_{j=1}^{n_u}$ and $\boldsymbol{\eta}$, and the time delays $\{\tau_j\}_{j=1}^{n_u}$ from the sampled input–output data $\{y(t_k),u_1(t_k),\ldots,u_{n_u}(t_k)\}_{k=1}^N$.

III. Proposed Methodology

In this section, a new method is proposed to estimate MISO time-delay models for MISO WPT systems based on the method developed in our previous paper [46]. To handle the scenario that the denominators associated with each input are not identical, an iterative multilinear regression technique [46], [47] is adopted.

Before going further, let us first define the prediction error cost function as follows:

$$J(\boldsymbol{\vartheta}) = \frac{1}{N}\sum_{k=1}^{N} \|\varepsilon(t_k, \boldsymbol{\vartheta})\|_2^2 \tag{23}$$

$$\varepsilon(t_k, \boldsymbol{\vartheta}) = \frac{1}{H(q^{-1}, \boldsymbol{\eta})}\left[y(t_k) - \sum_{j=1}^{n_u} G(p, \boldsymbol{\theta}_j) u_j(t_k - \tau_j)\right] \tag{24}$$

where $\boldsymbol{\vartheta} = [\boldsymbol{\theta}_1^\top, \tau_1, \ldots, \boldsymbol{\theta}_{n_u}^\top, \tau_{n_u}, \boldsymbol{\eta}^\top]^\top$ is a vector of the whole unknown parameters, and the optimization problem

$$\hat{\boldsymbol{\vartheta}} = \arg\min_{\boldsymbol{\vartheta}} J(\boldsymbol{\vartheta}). \tag{25}$$

Since the dimensionality of $\boldsymbol{\vartheta}$ can be high in the MISO setting, the optimization problem (25) will be solved in a separable fashion to avoid the problem of ill-conditioning, with the parameters associated with each plant model and the noise model being estimated separately. This strategy is benefited from the first and third conditions of Section II-D, which ensure a block-diagonal error covariance matrix of $\boldsymbol{\vartheta}$, i.e.,

$$P_{\boldsymbol{\vartheta}} = \begin{bmatrix} P_1 & & 0 \\ & \ddots & \\ 0 & & P_{n_u+1} \end{bmatrix} \tag{26}$$

each block P_j corresponding to the error covariance matrix of the pair $\{\boldsymbol{\theta}_j, \tau_j\}$ if $1 \leqslant j \leqslant n_u$, or $\boldsymbol{\eta}$ if $j = n_u + 1$. The above property allows us to estimate the parameters of each block separately.

A. Plant Model Parameter Estimation

The method of plant model estimation is based on the idea of decomposing a MISO model into n_u SISO models. Assuming that the output of the jth model is $y_j(t_k)$, and that $\boldsymbol{\eta}$ is known tentatively, the prediction error $\varepsilon(t_k, \boldsymbol{\vartheta})$ can be formulated in the following multilinear regression form [46]:

$$\begin{aligned}\varepsilon(t_k, \boldsymbol{\vartheta}) &= \sum_{j=1}^{n_u} \frac{1}{H(q^{-1}, \boldsymbol{\eta})}\left[y_j(t_k) - G(p, \boldsymbol{\theta}_j) u_j(t_k - \tau_j)\right] \\ &= \sum_{j=1}^{n_u} \frac{1}{A(p, \boldsymbol{\theta}_j) H(q^{-1}, \boldsymbol{\eta})}[A(p, \boldsymbol{\theta}_j) y_j(t_k) \\ &\quad - B(p, \boldsymbol{\theta}_j) u_j(t_k - \tau_j)] \\ &= \sum_{j=1}^{n_u} \tilde{y}_j^{(n_j)}(t_k) - \tilde{\boldsymbol{\phi}}_j^\top(t_k, \tau_j)\boldsymbol{\theta}_j \end{aligned} \tag{27}$$

where the filtered regression vectors are of the form

$$\begin{aligned}\tilde{\boldsymbol{\phi}}_j^\top(t_k, \tau_j) = \Big[&-\tilde{y}_j^{(n_j-1)}(t_k), \ldots, -\tilde{y}_j(t_k), \\ &\tilde{u}_j^{(m_j)}(t_k - \tau_j), \ldots, \tilde{u}_j(t_k - \tau_j)\Big]\end{aligned} \tag{28}$$

in which $\tilde{z}_j(t_k)$, $z = y$ or u, stands for the filtered version of $z_j(t_k)$ using the hybrid filter $1/A(p, \boldsymbol{\theta}_j) \cdot 1/H(q^{-1}, \boldsymbol{\eta})$.

It is interesting to observe from (27) that the estimation of $\{\boldsymbol{\theta}_j\}_{j=1}^{n_u}$ can be facilitated by solving a set of n_u linear regression problems, each being simpler than the original problem. Unfortunately, this idea cannot be directly implemented, due to the requirement of $y_j(t_k)$, which is unmeasured (only $y(t_k)$ is measured), and $\boldsymbol{\theta}_j$, which is unknown *a priori*. This problem can be avoided by using a bootstrap procedure for implementation: namely, by constructing the filters and auxiliary models based on initial values $\boldsymbol{\theta}_j^*$ and τ_j^*, we have

$$\tilde{z}_j^{(i)}(t_k) = \frac{p^i}{A(p, \boldsymbol{\theta}_j^*)} \cdot \frac{1}{H(q^{-1}, \boldsymbol{\eta})} z_j(t_k),\ z = y \text{ or } u \tag{29}$$

$$y_j(t_k) = y(t_k) - \sum_{i=1, i\neq j}^{n_u} G(p, \boldsymbol{\theta}_i^*) u_i(t_k - \tau_i^*). \tag{30}$$

Filtering a signal in the CT domain using DT data requires knowledge of the intersample behavior: see [48] for more details on the digital implementation.

Based on the dataset $\{y_j(t_k), u_j(t_k)\}_{k=1}^N$, the vector of rational parameters of the jth SISO model $\boldsymbol{\theta}_j$ can be sequentially estimated by repeatedly applying an existing SISO modeling method, with τ_j being fixed. An RIV method of estimation is normally used, as in this article, because least-squares estimation generates biased estimates in the presence of measurement noise (due to the correlation between the regression vector and the measurement noise).

Without loss of generality, based on (27) and following [42], the instrumental variable (IV) estimates of the parameters and the time delay of each SISO model are defined to solve the following problem:

$$\begin{bmatrix}\hat{\boldsymbol{\theta}}_j \\ \hat{\tau}_j\end{bmatrix} = \arg\min_{\boldsymbol{\theta}_j, \tau_j} \left\| \sum_{k=1}^{N} \begin{bmatrix}\hat{\tilde{\boldsymbol{\phi}}}_j(t_k) \\ \hat{\tilde{\psi}}_j(t_k)\end{bmatrix} \left[\tilde{y}_j^{(n_j)}(t_k) - \tilde{\boldsymbol{\phi}}_j^\top(t_k, \tau_j)\boldsymbol{\theta}_j\right] \right\|_2^2 \tag{31}$$

where $\hat{\tilde{\boldsymbol{\phi}}}_j(t_k)$ and $\hat{\tilde{\psi}}_j(t_k)$ are the instruments used in the estimation of $\boldsymbol{\theta}_j$ and τ_j, respectively. The problem (31) is also solved in a separable fashion according to [33], and further details are given in the next two subsections.

1) Rational Model Parameter Estimation: When τ_j is assumed to be fixed tentatively, an IV estimate of $\boldsymbol{\theta}_j$ as a function of τ_j is readily computed as

$$\hat{\boldsymbol{\theta}}_j(\tau_j) = \left[\sum_{k=1}^{N} \hat{\tilde{\boldsymbol{\phi}}}_j(t_k)\tilde{\boldsymbol{\phi}}_j^\top(t_k, \tau_j)\right]^{-1} \sum_{k=1}^{N} \hat{\tilde{\boldsymbol{\phi}}}_j(t_k)\tilde{y}_j^{(n_j)}(t_k). \tag{32}$$

According to the criterion that the instrument should be maximally correlated with the regression vector but uncorrelated with the noise, the RIV method, which is one of the most successful implementation of the IV techniques, uses the following instrument [28]:

$$\begin{aligned}\hat{\tilde{\boldsymbol{\phi}}}_j^\top(t_k) = \Big[&-\hat{\tilde{x}}_j^{(n_j-1)}(t_k), \ldots, -\hat{\tilde{x}}_j(t_k), \\ &\tilde{u}_j^{(m_j)}(t_k - \tau_j^*), \ldots, \tilde{u}_j(t_k - \tau_j^*)\Big]\end{aligned} \tag{33}$$

where $\hat{\tilde{x}}_j(t_k)$ is the noise-free version of $\tilde{y}_j(t_k)$ generated by the following auxiliary model parameterized by $\boldsymbol{\theta}_j^*$ and τ_j^*:

$$\hat{\tilde{x}}_j(t_k) = G(p, \boldsymbol{\theta}_j^*)\tilde{u}_j(t_k - \tau_j^*). \tag{34}$$

2) Time-Delay Estimation: By substituting (32) into (31), the optimization problem reduces to

$$\hat{\tau}_j = \arg\min_{\tau_j} \left\| \sum_{k=1}^{N} \hat{\tilde{\boldsymbol{\psi}}}_j(t_k) \left[\tilde{y}_j^{(n_j)}(t_k) - \tilde{\boldsymbol{\phi}}_j^{\top}(t_k, \tau_j)\hat{\boldsymbol{\theta}}_j(\tau_j) \right] \right\|_2^2. \tag{35}$$

As τ_j is nonlinear in the above expression, a gradient-based searching procedure can be employed for optimization

$$\hat{\tau}_j = \tau_j^* - \mu \left[\nabla^2 \breve{J}(\tau_j^*) \right]^{-1} \nabla \breve{J}(\tau_j^*) \tag{36}$$

where μ is a scaling factor that defines the step length; $\nabla \breve{J}(\tau_j)$ and $\nabla^2 \breve{J}(\tau_j)$ are the gradient and Hessian, respectively, which can be approximated as

$$\nabla \breve{J}(\tau_j) = -\sum_{k=1}^{N} \hat{\tilde{\boldsymbol{\psi}}}_j(t_k)\breve{\varepsilon}_j(t_k, \tau_j) \tag{37}$$

$$\nabla^2 \breve{J}(\tau_j) = -\sum_{k=1}^{N} \hat{\tilde{\boldsymbol{\psi}}}_j(t_k)\frac{\partial \breve{\varepsilon}_j(t_k, \tau_j)}{\partial \tau_j} \tag{38}$$

where $\breve{\varepsilon}_j(t_k, \tau_j) = \tilde{y}_j^{(n_j)}(t_k) - \tilde{\boldsymbol{\phi}}_j^{\top}(t_k, \tau_j)\hat{\boldsymbol{\theta}}_j(\tau_j)$. Following (27) and (32), the partial derivative $-\partial \breve{\varepsilon}_j(t_k, \tau_j)/\partial \tau_j$ involved in the above equation is computed as

$$\begin{aligned} -\frac{\partial \breve{\varepsilon}_j(t_k, \tau_j)}{\partial \tau_j} &= \frac{\partial \tilde{\boldsymbol{\phi}}_j^{\top}(t_k, \tau_j)}{\partial \tau_j}\hat{\boldsymbol{\theta}}_j(\tau_j) + \tilde{\boldsymbol{\phi}}_j^{\top}(t_k, \tau_j)\frac{d\hat{\boldsymbol{\theta}}_j(\tau_j)}{d\tau_j} \\ &= \frac{\partial \tilde{\boldsymbol{\phi}}_j^{\top}(t_k, \tau_j)}{\partial \tau_j}\hat{\boldsymbol{\theta}}_j(\tau_j) - \tilde{\boldsymbol{\phi}}_j^{\top}(t_k, \tau_j) \\ &\quad \cdot \left[\sum_{k=1}^{N} \hat{\tilde{\boldsymbol{\phi}}}_j(t_k)\tilde{\boldsymbol{\phi}}_j^{\top}(t_k, \tau_j) \right]^{-1} \\ &\quad \cdot \sum_{k=1}^{N} \hat{\tilde{\boldsymbol{\phi}}}_j(t_k)\frac{\partial \tilde{\boldsymbol{\phi}}_j^{\top}(t_k, \tau_j)}{\partial \tau_j}\hat{\boldsymbol{\theta}}_j(\tau_j). \end{aligned} \tag{39}$$

Letting $\tilde{\boldsymbol{\psi}}_j^{\top}(t_k, \tau_j) = [\partial \tilde{\boldsymbol{\phi}}_j^{\top}(t_k, \tau_j)/\partial \tau_j]\hat{\boldsymbol{\theta}}_j(\tau_j)$, we have

$$\begin{aligned} \nabla^2 \breve{J}(\tau_j) = &\sum_{k=1}^{N} \hat{\tilde{\boldsymbol{\psi}}}_j(t_k)\tilde{\boldsymbol{\psi}}_j^{\top}(t_k, \tau_j) - \sum_{k=1}^{N} \hat{\tilde{\boldsymbol{\psi}}}_j(t_k)\tilde{\boldsymbol{\phi}}_j^{\top}(t_k, \tau_j) \\ &\cdot \left[\sum_{k=1}^{N} \hat{\tilde{\boldsymbol{\phi}}}_j(t_k)\tilde{\boldsymbol{\phi}}_j^{\top}(t_k, \tau_j) \right]^{-1} \\ &\cdot \sum_{k=1}^{N} \hat{\tilde{\boldsymbol{\phi}}}_j(t_k)\tilde{\boldsymbol{\psi}}_j^{\top}(t_k, \tau_j). \end{aligned} \tag{40}$$

The final remaining question is how to choose the instrument $\hat{\tilde{\boldsymbol{\psi}}}_j(t_k)$. Motivated by (33) that $\hat{\tilde{\boldsymbol{\phi}}}_j^{\top}(t_k)$ is, in fact, the noise-free version of the partial derivative of $-\varepsilon(t_k, \boldsymbol{\vartheta})$ with respect to $\boldsymbol{\theta}_j$, evaluated at $\boldsymbol{\theta}_j^*$, and τ_j^*, $\hat{\tilde{\boldsymbol{\psi}}}_j(t_k)$ can be chosen as

$$\begin{aligned} &\hat{\tilde{\boldsymbol{\psi}}}_j(t_k) \\ &= -\frac{\partial \varepsilon(t_k, \boldsymbol{\vartheta})}{\partial \tau_j}\bigg|_{\boldsymbol{\theta}_j = \boldsymbol{\theta}_j^*, \tau_j = \tau_j^*} \\ &= \frac{\partial \tilde{\boldsymbol{\phi}}_j^{\top}(t_k, \tau_j)}{\partial \tau_j}\boldsymbol{\theta}_j^*\bigg|_{\tau_j = \tau_j^*} \\ &= -\left[0, \ldots, 0, \tilde{u}_j^{(m_j+1)}(t_k - \tau_j^*), \ldots, \tilde{u}_j^{(1)}(t_k - \tau_j^*) \right] \boldsymbol{\theta}_j^* \\ &= -\left[pG(p, \boldsymbol{\theta}_j^*)/H(q^{-1}, \boldsymbol{\eta}) \right] u_j(t_k - \tau_j^*) \end{aligned} \tag{41}$$

where the relation $\partial \tilde{u}_j(t - \tau_j)/\partial \tau_j = -\partial u_j(t - \tau_j)/\partial t$ has been used in deriving the third equality of the above equation.

Finally, on convergence, the estimation error covariance matrix can be computed according to [42] as follows:

$$P_{\boldsymbol{\theta}_j} = \sigma_{\varepsilon}^2 \left[\sum_{k=1}^{N} \hat{\tilde{\boldsymbol{\phi}}}_j(t_k)\hat{\tilde{\boldsymbol{\phi}}}_j^{\top}(t_k) \right]^{-1} \tag{42}$$

$$\begin{aligned} P_{\tau_j} = \sigma_{\varepsilon}^2 \Bigg\{ &\sum_{k=1}^{N} \hat{\tilde{\boldsymbol{\psi}}}_j(t_k)\hat{\tilde{\boldsymbol{\psi}}}_j^{\top}(t_k) - \sum_{k=1}^{N} \hat{\tilde{\boldsymbol{\psi}}}_j(t_k)\hat{\tilde{\boldsymbol{\phi}}}_j^{\top}(t_k) \\ &\cdot \left[\sum_{k=1}^{N} \hat{\tilde{\boldsymbol{\phi}}}_j(t_k)\hat{\tilde{\boldsymbol{\phi}}}_j^{\top}(t_k) \right]^{-1} \sum_{k=1}^{N} \hat{\tilde{\boldsymbol{\phi}}}_j(t_k)\hat{\tilde{\boldsymbol{\psi}}}_j^{\top}(t_k) \Bigg\}^{-1} \end{aligned} \tag{43}$$

where σ_{ε}^2 is the variance of the prediction error. From the above two equations, it is clear that the uncertainties on the estimated parameters are always decreasing with sample size and can be made vanishing small when the number of data points tends to infinity.

B. Noise Model Parameter Estimation

When the plant model parameters have been obtained, the colored measurement noise can be estimated as

$$\hat{\xi}(t_k) = y(t_k) - \sum_{j=1}^{n_u} G(p, \hat{\boldsymbol{\theta}}_j)u_i(t_k - \hat{\tau}_j). \tag{44}$$

Then, based on the estimated sequence $\{\hat{\xi}(t_k)\}_{k=1}^{N}$, standard routines can be used to estimate the vector of ARMA model parameters $\boldsymbol{\eta}$, such as that used in [42].

C. Complete Algorithm

The complete algorithm of the proposed method, referred to as refined instrumental variable for continuous-time transfer function (TFRIVC[1]) models, is summarized in Algorithm 1.

IV. Practical Considerations

For successful application of the proposed method to model WPT systems, the initial settings have to be properly specified.

[1]The TFRIVC method will be included in the CONTSID toolbox, which can be downloaded from http://www.cran.univ-lorraine.fr/contsid/

Algorithm 1: Basic TFRIVC Method.

Input:
- Sampled data: $\{y(t_k), u_1(t_k), \ldots, u_{n_u}(t_k)\}_{k=1}^{N}$;
- Polynomial degrees: $\{n_j, m_j\}_{j=1}^{n_u}$, n_c, n_d;
- Initial parameter vector: $\boldsymbol{\vartheta}^*$;
- Maximum iteration number: $N_{\max}$;
- Tolerances of cost and parameter changes: ς_{fun}, ς_{par};
- Lower and upper time-delay boundaries: $\{\underline{\tau}_j, \overline{\tau}_j\}_{j=1}^{n_u}$;

Output: $\boldsymbol{\vartheta}^*$;

for $r \leftarrow 1$ **to** $N_{\max}$ **do**
  $\mu \leftarrow 1$;
  for $j \leftarrow 1$ **to** n_u **do**
    compute $y_j(t_k)$ in (30), $\nabla J(\tau_j^*)$ in (37), and $\nabla^2 J(\tau_j^*)$ in (38) using $\boldsymbol{\vartheta}^*$;
    compute the time-delay increment $\Delta\tau_j \leftarrow \left[\nabla^2 \breve{J}(\tau_j^*)\right]^{-1} \nabla \breve{J}(\tau_j^*)$;
    while $\tau_j^* - \mu\Delta\tau_j \notin [\underline{\tau}_j, \overline{\tau}_j]$ **do** $\mu \leftarrow \mu/2$;
  end
  for $i \leftarrow 1$ **to** $N_{\max}$ **do**
    for $j \leftarrow 1$ **to** n_u **do**
      update the time delay: $\hat{\tau}_j \leftarrow \tau_j^* - \mu\Delta\tau_j$;
      compute $\tilde{\boldsymbol{\phi}}_j^{\top}(t_k, \hat{\tau}_j)$ in (28), $\tilde{y}_j^{(n_j)}(t_k)$ in (29), and $\hat{\tilde{\boldsymbol{\phi}}}_j^{\top}(t_k)$ in (33) using $\boldsymbol{\theta}_j^*$ and $\hat{\tau}_j$;
      generate $\hat{\boldsymbol{\theta}}_j$ using the IV estimator

$$\hat{\boldsymbol{\theta}}_j \leftarrow \left[\sum_{k=1}^{N} \hat{\tilde{\boldsymbol{\phi}}}_j(t_k)\tilde{\boldsymbol{\phi}}_j^{\top}(t_k, \hat{\tau}_j)\right]^{-1} \cdot \sum_{k=1}^{N} \hat{\tilde{\boldsymbol{\phi}}}_j(t_k)\tilde{y}_j^{(n_j)}(t_k);$$

    end
    compute $\hat{\xi}(t_k)$ in (44) using $\{\hat{\boldsymbol{\theta}}_j, \hat{\tau}_j\}_{j=1}^{n_u}$ and, based on which, generate $\hat{\boldsymbol{\eta}}$ using an ARMA estimation routine;
    compute the cost $J(\hat{\boldsymbol{\vartheta}})$ in (23);
    if $J(\hat{\boldsymbol{\vartheta}}) \geqslant J(\boldsymbol{\vartheta}^*)$ **then**
      $\mu \leftarrow \mu/2$;
      if $\|\Delta\boldsymbol{\vartheta}^*./\boldsymbol{\vartheta}^*\| < \varsigma_{\text{par}}$ **then** break;
    else
      $\boldsymbol{\vartheta}^* \leftarrow \hat{\boldsymbol{\vartheta}}$;
      break;
    end
  end
  if $|\Delta J(\boldsymbol{\vartheta}^*)/J(\boldsymbol{\vartheta}^*)| < \varsigma_{\text{fun}}$ or $\|\Delta\boldsymbol{\vartheta}^*./\boldsymbol{\vartheta}^*\| < \varsigma_{\text{par}}$ **then** break;
end

These include: 1) how to determine the polynomial degrees $\{n_j, m_j\}_{j=1}^{n_u}$, n_c and n_d; 2) how to select the initial parameters, since the proposed method is a bootstrap procedure; and 3) how to determine the upper and lower boundaries of the time delays.

A. Choice of Polynomial Degrees

For the WPT system under consideration, there are two main operating modes.

1) If the driving frequency of the system is exactly equal to the resonant frequency, all resonators of the circuit become resistive, so that the output filtering capacitor C_f is the only reactive component in the circuit. In this sense, it is straightforward that the model of the system is of first order, i.e., $n_j = 1, m_j = 0, j = 1, \ldots, n_u$. The idea used for model order selection follows the concept of data-based mechanistic modeling introduced in (see [42, Ch. 12] and the prior references therein), which searches for and identifies the dominant physical mechanism governing the system's dynamic behavior and investigates how this can be modeled in the simplest manner.
2) If driving frequency of the system is slightly larger than the resonant frequency, the inductive behaviors of the resonators are not fully compensated for by the capacitor connected in series. In this situation, the resonant tank is inductive, and thus, the whole circuit could be explained by a second-order model, i.e., $n_j = 2$, and $m_j = 0$ or 1, as long as the driving-resonant frequency mismatch is not very large. Note that, while a high-order model can have better explanatory ability, this is not necessarily attractive in control system design terms, since low-order models are always preferred for such design purposes if they provide a sufficiently accurate description of the system dynamics.

Practical WPT systems normally work at the second mode to protect the switching devices from damage. Therefore, a simple plant model up to order 2 is always enough for dynamic modeling (see also [25]). A simpler way to help select the model order is to observe the waveform of the output response: if there is a clear oscillation in this response, a second-order model is suggested; otherwise, a first-order model is preferred. On the other hand, the choice of n_c and n_d can be achieved, as normal in time-series analysis, by reference to statistical measures, such as the coefficient of determination R_T^2 and model order identification criteria (see [28] and [46]). One should also be aware that the choice of n_c and n_d is not critical, since the proposed IV method is able to generate statistically consistent estimates, even if the noise model is not correctly specified (although their correct identification ensures lower variance estimates). However, the topic of time-series analysis is out of the scope of this article, and the interested reader is advised to refer to books such as [28] for more details.

B. Choice of Initial Parameters

To initiate the proposed bootstrap estimation procedure, initial parameters $\{\boldsymbol{\theta}_j^*, \tau_j^*\}$ are required in order to compute the filtered signals in (29) and (30), as well as the gradient and Hessian in (36). To this end, two methods are suggested to generate $\{\boldsymbol{\theta}_j^*\}$ when the time delays are assumed to be known.

1) *Circuit-theory-based method:* This method is preferred when the experimenter has an enough *a priori* information about the circuit topology and component parameters.
2) *State variable filter-based IV (IVSVF) method:* This is a more user-friendly data-driven method, requiring only a few initial settings, i.e., the cutoff frequency of the state variable filter λ, and the polynomial degrees $\{n_j, m_j\}_{j=1}^{n_u}$.

Algorithm 2: IVSVF Method.

Input:
- Sampled data: $\{y(t_k), u_1(t_k), \ldots, u_{n_u}(t_k)\}_{k=1}^{N}$;
- Polynomial degrees: $\{n_j, m_j\}_{j=1}^{n_u}$;
- Cutoff frequency: λ;
- Initial time delays: $\{\tau_j^*\}_{j=1}^{n_u}$;

Output: $\{\boldsymbol{\theta}_j^*\}_{j=1}^{n_u}$;

for $j \leftarrow 1$ **to** n_u **do**
- $y_j(t_k) \leftarrow y(t_k)$;
- compute $\tilde{\boldsymbol{\phi}}_j^\top(t_k, \tau_j^*)$ in (28) and $\tilde{y}_j^{(n_j)}(t_k)$ in (29) using $L(p) = 1/(p+\lambda)^{n_j}$;
- generate $\boldsymbol{\theta}_j^*$ using the LS estimator

$$\boldsymbol{\theta}_j^* \leftarrow \left[\sum_{k=1}^{N} \tilde{\boldsymbol{\phi}}_j(t_k, \tau_j^*)\tilde{\boldsymbol{\phi}}_j^\top(t_k, \tau_j^*)\right]^{-1} \cdot \sum_{k=1}^{N} \tilde{\boldsymbol{\phi}}_j(t_k, \tau_j^*)\tilde{y}_j^{(n_j)}(t_k);$$

end

for $j \leftarrow 1$ **to** n_u **do**
- compute $y_j(t_k)$ in (30) using $\{\boldsymbol{\theta}_j^*, \tau_j^*\}_{j=1}^{n_u}$;
- compute $\tilde{\boldsymbol{\phi}}_j^\top(t_k, \tau_j^*)$ in (28), $\tilde{y}_j^{(n_j)}(t_k)$ in (29), and $\hat{\tilde{\boldsymbol{\phi}}}_j^\top(t_k)$ in (33) using $\boldsymbol{\theta}_j^*$ and τ_j^*;
- refine $\boldsymbol{\theta}_j^*$ using the IV estimator

$$\boldsymbol{\theta}_j^* \leftarrow \left[\sum_{k=1}^{N} \hat{\tilde{\boldsymbol{\phi}}}_j(t_k)\tilde{\boldsymbol{\phi}}_j^\top(t_k, \tau_j^*)\right]^{-1} \cdot \sum_{k=1}^{N} \hat{\tilde{\boldsymbol{\phi}}}_j(t_k)\tilde{y}_j^{(n_j)}(t_k);$$

end

Further details on the first method are given in [25], while the latter method is summarized in Algorithm 2. The selection of $\{\tau_j^*\}$ should be carried out with special care, since the cost function is always nonconvex with respect to the time delays. As a consequence, the estimation procedure is possibly trapped by local minima if initial time delays are far from the global optima. In order to relieve this problem, it is suggested that a grid of initial time delay values is used. Then, we estimate a rational model at each grid point, using the IVSVF method with the time delays being fixed; subsequently, among the resulting models, the one that has the minimal cost is used as the initial model for the basic TFRIVC method. One the other hand, the choice of λ is not very critical if the initial time delays are determined using a grid search, and convergence can occur for a fairly wide range of values. The above discussion leads to a more robust implementation of TFRIVC (see Algorithm 3).

C. Choice of Time-Delay Boundaries

The choice of time-delay boundaries in the SISO scenario has been discussed in our previous paper [25]. By default, one can simply let $\underline{\tau}_j = 0$ if no *a priori* knowledge is available, while the upper boundary can be computed based on sampled input–output data by minimizing the following cross-correlation function:

$$\overline{\tau}_j = \arg\max_{\tau_j} \left|\mathbb{E}\left\{y_j(t_k)u_j(t_k - \tau_j)\right\}\right| \tag{45}$$

where $\mathbb{E}$ is the expectation operator. Note that the resulting $\overline{\tau}_j$ is always larger than the true time delay if the system is causal [25]. However, there is a difficulty in direct implementation of (45), due to the unknown $y_j(t_k)$ in the MISO scenario. To circumvent this problem, it is suggested that $\{\boldsymbol{\theta}_j\}$ is estimated using the simpler IVSVF method (see previous references) by setting the time delays to the lower boundaries and, subsequently, computing $y_j(t_k)$ using (30), based on the models obtained from sampled data.

Algorithm 3: Robust TFRIVC Method.

Input:
- Sampled data: $\{y(t_k), u_1(t_k), \ldots, u_{n_u}(t_k)\}_{k=1}^{N}$;
- Polynomial degrees: $\{n_j, m_j\}_{j=1}^{n_u}$, n_c, n_d;
- Cutoff frequency: λ;
- Number of time delays to be compared: $\{K_j\}_{j=1}^{n_u}$;
- Maximum iteration number: $N_{\max}$;
- Tolerances of cost and parameter changes: ς_{fun}, ς_{par};
- Lower and upper time-delay boundaries: $\{\underline{\tau}_j, \overline{\tau}_j\}_{j=1}^{n_u}$;

Output: $\boldsymbol{\vartheta}^*$;

define $\boldsymbol{\vartheta} = \left[\boldsymbol{\theta}_1^\top, \tau_1, \ldots, \boldsymbol{\theta}_{n_u}^\top, \tau_{n_u}\right]^\top$;

define the set of possible time-delay combinations:

$$S = \big\{(\tau_1, \ldots, \tau_{n_u}) : \tau_j = \underline{\tau}_j + i(\overline{\tau}_j - \underline{\tau}_j)/K_j; \; 0 \leqslant i \leqslant K_j; 1 \leqslant j \leqslant n_u\big\};$$

set initial time delays: $\{\hat{\tau}_j\}_{j=1}^{n_u} \leftarrow \{\underline{\tau}_j\}_{j=1}^{n_u}$;

apply the IVSVF algorithm to generate $\{\hat{\boldsymbol{\theta}}_j\}_{j=1}^{n_u}$;

$\boldsymbol{\vartheta}^* \leftarrow \hat{\boldsymbol{\vartheta}}$;

foreach $(\tau_1, \ldots, \tau_{n_u}) \in S$ **do**
- **for** $j \leftarrow 1$ **to** n_u **do**
  - compute $y_j(t_k)$ in (30) using $\{\hat{\boldsymbol{\theta}}_j, \hat{\tau}_j\}_{j=1}^{n_u}$;
- **end**
- **for** $j \leftarrow 1$ **to** n_u **do**
  - $\hat{\tau}_j \leftarrow \tau_j$;
  - compute $\tilde{\boldsymbol{\phi}}_j^\top(t_k, \hat{\tau}_j)$ in (28), $\tilde{y}_j^{(n_j)}(t_k)$ in (29), and $\hat{\tilde{\boldsymbol{\phi}}}_j^\top(t_k)$ in (33) using $\hat{\boldsymbol{\theta}}_j$ and $\hat{\tau}_j$;
  - update $\hat{\boldsymbol{\theta}}_j$ using the IV estimator

$$\hat{\boldsymbol{\theta}}_j \leftarrow \left[\sum_{k=1}^{N} \hat{\tilde{\boldsymbol{\phi}}}_j(t_k)\tilde{\boldsymbol{\phi}}_j^\top(t_k, \hat{\tau}_j)\right]^{-1} \cdot \sum_{k=1}^{N} \hat{\tilde{\boldsymbol{\phi}}}_j(t_k)\tilde{y}_j^{(n_j)}(t_k);$$

- **end**
- compute $J(\hat{\boldsymbol{\vartheta}})$ in (23) with $H(q^{-1}, \boldsymbol{\eta}) = 1$;
- **if** $J(\hat{\boldsymbol{\vartheta}}) < J(\boldsymbol{\vartheta}^*)$ **then** $\boldsymbol{\vartheta}^* \leftarrow \hat{\boldsymbol{\vartheta}}$;

end

compute $\hat{\xi}(t_k)$ in (44) using $\boldsymbol{\vartheta}^*$ and, based on which, generate $\boldsymbol{\eta}^*$ using an ARMA estimation routine;

$\boldsymbol{\vartheta}^* \leftarrow \left[(\boldsymbol{\vartheta}^*)^\top, (\boldsymbol{\eta}^*)^\top\right]^\top$;

apply the basic TFRIVC algorithm (see Algorithm 1) to refine $\boldsymbol{\vartheta}^*$;

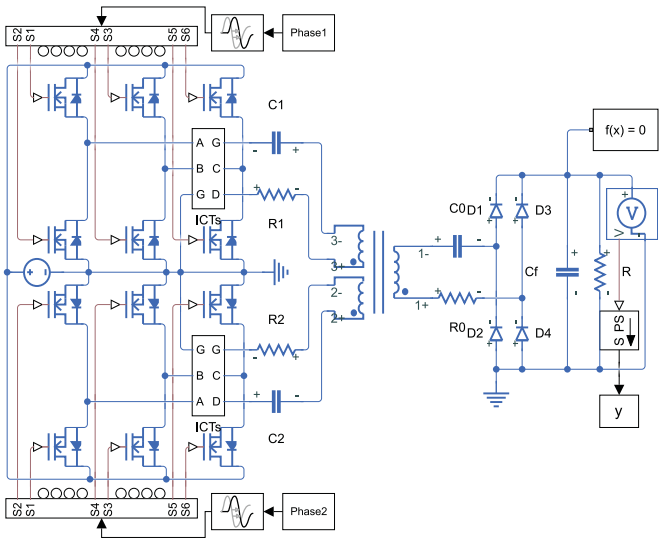

Fig. 10. Simscape diagram for a two-input WPT system. In the two ICT subsystems, A, B, and C are the three inputs of the ICT windings, D is the output of the ICT windings, and the two Gs are interconnected.

TABLE I
MAIN PARAMETERS OF THE SIMSCAPE DIAGRAM IN FIG. 10

Parameter	Explanation	Value
C_0	Capacitance of the receiver resonator	40 nF
C_1	Capacitance of the 1st transmitter resonator	40 nF
C_2	Capacitance of the 2nd transmitter resonator	40 nF
C_f	Capacitance of the output filter	2200 μF
f_s	Driving frequency of the inverters	80 kHz
L_0	Inductance of the receiver resonator	105 μH
L_1	Inductance of the 1st transmitter resonator	105 μH
L_2	Inductance of the 2nd transmitter resonator	105 μH
L_{ict}	Inductance of each ICT winding	5 μH
$M_{1,0}$	Mutual inductance between L_1 and L_0	1.83 μH
$M_{1,0}$	Mutual inductance between L_2 and L_0	5.50 μH
$M_{2,1}$	Mutual inductance between L_2 and L_1	-0.1 μH
M_{ict}	Mutual inductance between coupled L_{ict}'s	4.9 μH
R	Load resistance	5 Ω
R_0	Equivalent resistance of the L_0, C_0 branch	100 mΩ
R_1	Equivalent resistance of the L_1, C_1 branch	100 mΩ
R_2	Equivalent resistance of the L_2, C_2 branch	100 mΩ
R_s	On-state resistance of the switches	1 mΩ
τ_1	Delay of the 1st transmitter	4.5 ms
τ_2	Delay of the 2nd transmitter	1.5 ms
V_d	Voltage of the DC source	100 V
V_r	Forward voltage of the diodes	0.5 V

V. SIMULATION EXAMPLE

In this section, the effectiveness of the proposed method is illustrated by numerical simulation. The input–output data used for model estimation were generated by using Simscape in MATLAB; Fig. 10 depicts the circuit diagram. The system under consideration consisted of two phase-controlled three-phase inverters and one receiver, with the main circuit component parameters listed in Table I. The experiment was carried out in the following three steps.

1) First, the stationary inputs were initially set as $\overline{\Gamma}_1 = 0.52$ and $\overline{\Gamma}_2 = 0.46$, in order to establish a stationary working point. Here, the values stand for normalized phases, e.g., 0.52 corresponds to an actual phase angle of 93.6°. After the system had entered a steady state, the output voltage was measured to be 21.27 V.
2) Second, each input was perturbed by a test sequence to generate informative data for model identification. More specifically, $u_1(t)$ was chosen as a pseudorandom binary sequence (PRBS) generated from an eight-stage shift register at a clock period $5T$, while $u_2(t)$ was chosen as another PRBS generated from a seven-stage shift register at a clock period $10T$, where $T = 1$ ms is the sampling interval. Both PRBSs had the amplitude switching between ± 0.01. It will be seen from (49) that the bandwidths of the estimated models are 233.2 Hz for the first channel and 234.4 Hz for the second channel. The 1-kHz sampling frequency, approximately 4.29 times of the model bandwidth, is close to the range suggested in the end of Section II-C.
3) Third, as soon as the perturbations had been applied, the input–output signals were observed at time instant $t_k = kT, k = 1, 2, \ldots, 1280$. It was assumed that the input was noise-free, while the sampled output was corrupted by colored noise

$$y(t_k) = x(t_k) + \xi(t_k) \tag{46}$$

where $x(t_k)$ stands for the noise-free output, and $\xi(t_k)$ is a colored measurement noise that is a filtered version of white noise $e(t_k)$ through the following model:

$$\begin{aligned}\xi(t_k) &= H(q^{-1}, \boldsymbol{\eta})e(t_k) \\ &= \frac{1 + 0.2497q^{-1}}{1 - 0.9744q^{-1} + 0.2231q^{-2}}e(t_k).\end{aligned} \tag{47}$$

The variance of $e(t_k)$ was adjusted to achieve a signal-to-noise ratio (SNR) of 15 dB in the experiment, where SNR is defined as

$$\text{SNR} = 10\log_{10}\left(P_x/P_\xi\right) \text{ dB} \tag{48}$$

and P_x and P_ξ are the power of $x(t_k)$ and $\xi(t_k)$, respectively. Fig. 11 shows a portion of sampled data.

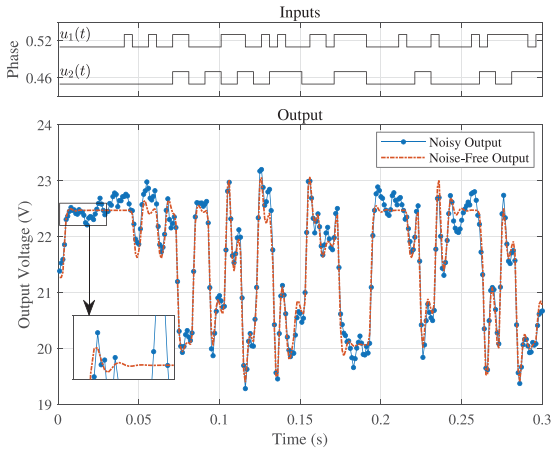

Fig. 11. Portion of the sampled input and output signals.

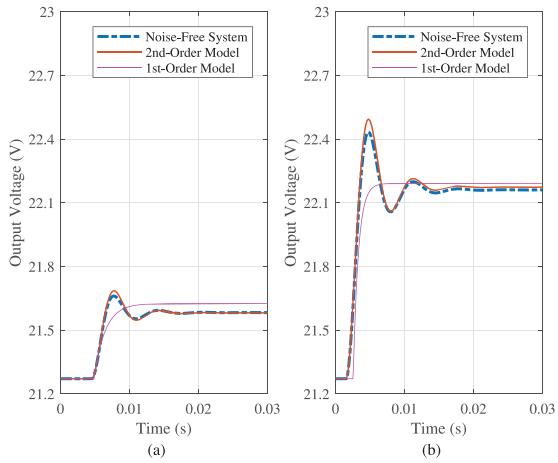

Fig. 12. Responses of the estimated first- and second-order models, when $u_1(t)$ steps from 0 to -0.01 at around the stationary point $\overline{I}_1 = 0.52$, and when $u_2(t)$ steps from 0 to -0.01 around the stationary point $\overline{I}_2 = 0.46$. (a) Step response from $u_1(t)$. (b) Step response from $u_2(t)$.

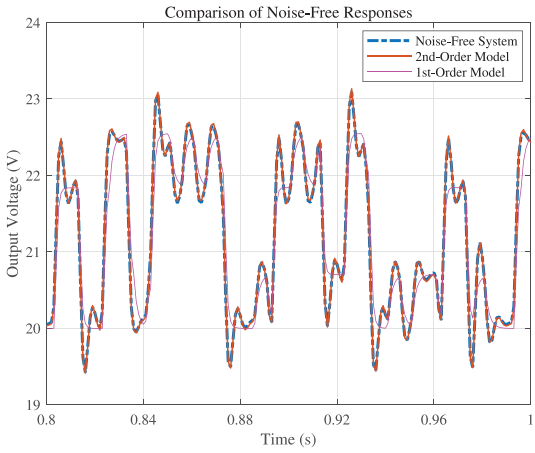

Fig. 13. Comparison of the noise-free responses of the estimated first- and second-order models.

Note that the model estimated by the proposed method is, in fact, a small-signal model, so that the stationary values should be removed from the data before they are used for model estimation. However, these stationary values should be retained when plotting the responses of the estimated models (see Figs. 12, 13, 17, and 18). According to the guidelines suggested in Section IV, the initial settings for the robust TFRIVC method were chosen as $n_1 = n_2 = 2$, $m_1 = m_2 = 0$, $n_c = 2$, $n_d = 1$, $\underline{\tau}_1 = \underline{\tau}_2 = 0$ s, $\overline{\tau}_1 = 8$ ms, $\overline{\tau}_2 = 5$ ms, $\lambda = 1000$ rad/s, and $K_1 = K_2 = 10$. The other parameters remained at their default values.

An interesting phenomenon, shown in the magnified part of Fig. 11, is that the system output has a clear oscillation when a step change is added to the input. This phenomenon can be explained by point 2 of Section IV-A: as the resonant frequency is $f_0 = 1/(2\pi\sqrt{L_0 C_0}) = 78$ kHz, the resonant tank is inductive at the driving frequency $f_s = 80$ kHz, so that the whole circuit may behave as an *LCR* oscillator, whose output response shows an oscillatory component. This is why a second-order model has been adopted to represent the system.

TABLE II
FIT RATIOS FOR THE ESTIMATED MODELS (49), (52), AND (54)

Model	Fit to noisy data	Fit to noise-free data
1st-order model (52)	67.42%	71.17%
2nd-order model (49)	82.76%	98.32%
3rd-order model (54)	82.78%	98.22%

The proposed robust TFRIVC method is called by the following statement:

$$\begin{aligned}[\mathtt{G},\mathtt{H}] = \mathtt{tfrivc}(&\mathtt{data}, [n_1, n_2], [m_1, m_2], \ldots \\ &'\mathtt{tdmin}', [\underline{\tau}_1, \underline{\tau}_2], '\mathtt{tdmax}', [\overline{\tau}_1, \overline{\tau}_2], \ldots \\ &'\mathtt{numtd}', [K_1, K_2], '\mathtt{lambda}', \lambda, \ldots \\ &'\mathtt{nn}', [n_c, n_d])\end{aligned}$$

where G and H denote the resulting plant and noise models, respectively, and data is an iddata object from the MATLAB system identification toolbox that contains the sampled input–output data. In a single-run experiment, the estimated second-order model is

$$\begin{aligned}x(t) = &\frac{-3.25 \cdot 10^7}{p^2 + 675p + 1.047 \cdot 10^6} u_1(t - 0.00449) \\ &+ \frac{-9.388 \cdot 10^7}{p^2 + 639.7p + 1.041 \cdot 10^6} u_2(t - 0.00152) \quad (49)\end{aligned}$$

$$\xi(t_k) = \frac{1 + 0.2162q^{-1}}{1 - 0.9978q^{-1} + 0.2678q^{-2}} e(t_k). \quad (50)$$

The accuracy of the above estimated model was evaluated by the performance index

$$\text{fit} = \left(1 - \frac{\|y(t_k) - y_s(t_k)\|_2}{\|y(t_k) - y_m(t_k)\|_2}\right) \cdot 100\% \quad (51)$$

where $y(t_k)$ is the sampled output, $y_s(t_k)$ is the simulated output generated from the estimated plant model, and $y_m(t_k)$ is the mean value of $y(t_k)$. The model response and the fit were computed using the compare routine from the MATLAB system identification toolbox.

For comparative purposes, we also present the estimated first-order model

$$\begin{aligned}x(t) = &\frac{-2.198 \cdot 10^4}{p + 620.4} u_1(t - 0.00484) \\ &+ \frac{-1.242 \cdot 10^5}{p + 1350} u_2(t - 0.00254) \quad (52)\end{aligned}$$

$$\xi(t_k) = \frac{1 + 0.3633q^{-1}}{1 - 1.207q^{-1} + 0.5791q^{-2}} e(t_k) \quad (53)$$

and the estimated third-order model

$$\begin{aligned}x(t) = &\frac{7170p^2 - 3.048 \cdot 10^7 p - 1.56 \cdot 10^7}{p^3 + 652p^2 + 1.007 \cdot 10^6 p + 6.287 \cdot 10^5} \\ &\cdot u_1(t - 0.00423) \\ &+ \frac{5242p^2 - 9.362 \cdot 10^7 p - 9.228 \cdot 10^6}{p^3 + 639.2p^2 + 1.038 \cdot 10^6 p + 2.127 \cdot 10^5} \\ &\cdot u_2(t - 0.00146) \quad (54)\end{aligned}$$

TABLE III
ESTIMATED SECOND-ORDER MODEL PARAMETERS

Method	Estimated parameters value (mean(±std))								$\overline{\text{fit}}$
	$\hat{a}_{1,1}$	$\hat{a}_{2,1}$	$\hat{b}_{0,1}$	$\hat{\tau}_1$	$\hat{a}_{1,2}$	$\hat{a}_{2,2}$	$\hat{b}_{0,2}$	$\hat{\tau}_2$	
SRIVC	666.9	$7.529 \cdot 10^5$	$-2.37 \cdot 10^7$	0.004	701.9	$1.44 \cdot 10^6$	$-1.28 \cdot 10^8$	0.002	79.74%
	(±54)	($\pm 2.08 \cdot 10^4$)	($\pm 1.4 \cdot 10^6$)	(±0)	(±20.8)	($\pm 2.2 \cdot 10^4$)	($\pm 3.11 \cdot 10^6$)	(±0)	(±0.35%)
TFRIVC	661.1	$1.041 \cdot 10^6$	$-3.231 \cdot 10^7$	0.004507	648.8	$1.04 \cdot 10^6$	$-9.276 \cdot 10^7$	0.001513	82.53%
	(±31.1)	($\pm 3.2 \cdot 10^4$)	($\pm 1.2 \cdot 10^6$)	($\pm 3.3 \cdot 10^{-5}$)	(±12.8)	($\pm 1.29 \cdot 10^4$)	($\pm 1.5 \cdot 10^6$)	($\pm 1.6 \cdot 10^{-5}$)	(±0.2%)

$\overline{\text{fit}}$—Mean fit value.

$$\xi(t_k) = \frac{1 + 0.2184q^{-1}}{1 - 0.9953q^{-1} + 0.265q^{-2}} e(t_k). \tag{55}$$

The fit ratios of the above three models in (49), (52), and (54) are listed in Table II, showing that the second-order model is more accurate than the first-order model, and it has almost the same accuracy as the third-order model. The responses of the estimated first- and second-order models when $u_1(t)$ steps from 0 to -0.01 at around the stationary point $\overline{\Gamma}_1 = 0.52$, and when $u_2(t)$ steps from 0 to -0.01 around the stationary point $\overline{\Gamma}_2 = 0.46$, are compared in Fig. 12. The noise-free outputs of the estimated first- and second-order models, in response to the sampled inputs, are compared in Fig. 13. Both figures confirm the accuracy of the estimated second-order model.

Subsequently, a Monte–Carlo (MC) simulation of 100 independent runs was conducted to show the statistical properties of the parameter estimates. In order to evaluate the quality of the results further, the simpler standard SRIVC routine available from the CONTSID toolbox was implemented to show the improvement of the proposed fractional time-delay estimation method. SRIVC can be called in the following way to estimate the parameters of a first-order two-input single-output model with known time delays:

$$\texttt{G} = \texttt{srivc}(\texttt{data}, [m_1, m_2, n_1, n_2, n_{k,1}, n_{k,2}]);$$

where $n_{k,j}$, $j = 1$ or 2, constrained to be an integer number of sampling intervals, is the time delay of the jth input channel. By trial and error, it was found that the optimal values were $n_{k,1} = 4$ and $n_{k,2} = 2$ for this example.

For each MC run, the WPT system was initially in a stationary state, so the initial model state was set to zero during the model estimation process. The parameter estimates generated by the SRIVC and TFRIVC methods from the 100 MC runs are listed in Table III, from which it is clear that SRIVC performs quite well here because good integer time delays have been given to the algorithm, while TFRIVC improves the fit ratio by 2.79% compared with SRIVC, thanks to its capability of estimating fractional time delays. Note that the estimated noise model parameters by TFRIVC are not shown in this table, due to the space constraints.

VI. EXPERIMENTAL EXAMPLE

In this section, the effectiveness of the proposed method was evaluated using real data generated by the experimental apparatus shown in Fig. 14. In order to show the versatility of the proposed method for the identification of WPT systems supplied

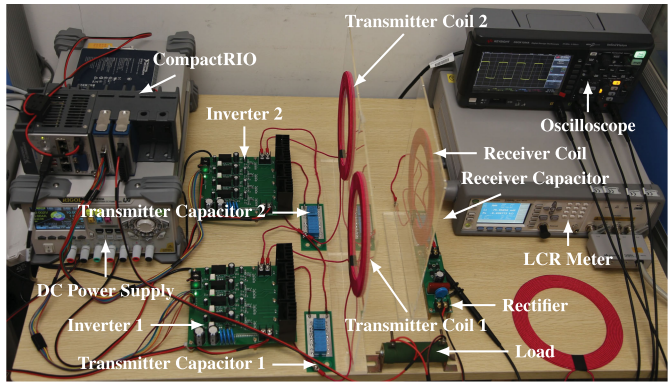

Fig. 14. Experimental apparatus.

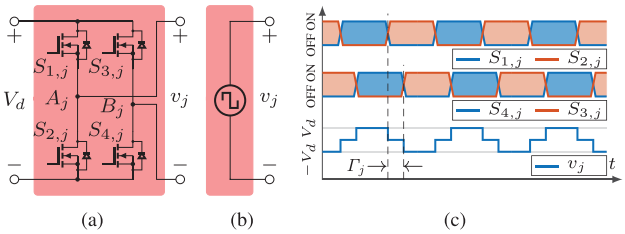

Fig. 15. Full-bridge inverter. (a) Circuit diagram. (b) Equivalent circuit. (c) Signal waveforms.

by different types of inverters, two phase-controlled full-bridge inverters were used in the experiment to power a single receiver. The inverter output has the following analytical expression:

$$\begin{aligned} v_j &= v_{a,j} - v_{b,j} \\ &\approx \frac{2V_d}{\pi}\left[\sin\left(\omega_s t + \frac{\Gamma_j}{2}\right) - \sin\left(\omega_s t - \pi - \frac{\Gamma_j}{2}\right)\right] \\ &= \frac{4V_d}{\pi}\cos\left(\frac{\Gamma_j}{2}\right) \cdot \sin(\omega_s t) \end{aligned} \tag{56}$$

where, in Fig. 15, $v_{a,j}$ and $v_{b,j}$ denote the voltages at points A_j and B_j, respectively, and Γ_j is the phase shift. Compared with the three-phase inverter, the input nonlinearity of the full-bridge inverter is clearly

$$f(\Gamma_j) = \cos\left(\frac{\Gamma_j}{2}\right). \tag{57}$$

The measurement and control was implemented on a National Instruments (NI) CompactRIO system, which had two built-in controllers: a 1.33-GHz Intel Atom CPU, and a Kintex-7

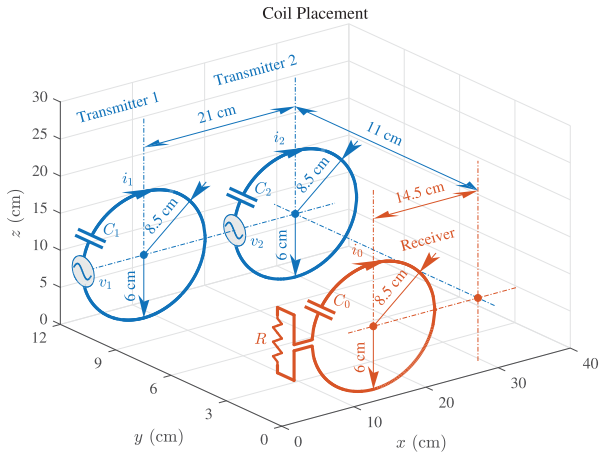

Fig. 16. Coil placement.

TABLE IV
MAIN PARAMETERS OF THE EXPERIMENTAL APPARATUS

Parameter	Explanation	Value
C_0	Capacitance of the receiver resonator	37.76 nF
C_1	Capacitance of the 1st transmitter resonator	38.59 nF
C_2	Capacitance of the 2nd transmitter resonator	38.06 nF
C_f	Capacitance of the output filter	471.2 μF
f_s	Driving frequency of the inverters	80 kHz
L_0	Inductance of the receiver resonator	104.3 μH
L_1	Inductance of the 1st transmitter resonator	104.4 μH
L_2	Inductance of the 2nd transmitter resonator	105.2 μH
$M_{1,0}$	Mutual inductance between L_1 and L_0	4.234 μH
$M_{2,0}$	Mutual inductance between L_2 and L_0	2.224 μH
$M_{2,1}$	Mutual inductance between L_2 and L_1	-1.823 μH
R	Load resistance	9.7 Ω
R_0	Equivalent resistance of the L_0, C_0 branch	162.4 mΩ
R_1	Equivalent resistance of the L_1, C_1 branch	161.1 mΩ
R_2	Equivalent resistance of the L_2, C_2 branch	162.0 mΩ
R_s	On-state resistance of the switches	12.6 mΩ
V_d	Voltage of the DC source	7 V
V_r	Forward voltage of the diodes	0.5 V

70T field-programmable gate array (FPGA). The full-bridge inverters were composed of four Texas Instruments CSD19534 N-channel MOSFETs, whose typical drain-to-source voltage and drain current were 100 V and 10 A, respectively. The pulsewidth modulation (PWM) signals to drive these MOSFETs were generated by the interval FPGA of CompactRIO and exported by an NI-9401, which was a 5-V/TTL, eight-bidirectional-channel, 100-ns digital module. The output voltage was measured by the CPU via an NI-9201, which was a $\pm$10-V, 500-kS/s, 12-bit, eight-channel voltage input module.

The three resonators had the same design parameters: all coils were round and made by Litz wire of 1200 strands, each strand having a diameter of 0.01 mm, in order to relieve the skin effect. Moreover, the number of coil turns was 21, with the outer and inner diameters of 17 and 12 cm, respectively. The vertical distances between the transmitter and receiver coil planes were 11 cm. Fig. 16 depicts further details about the coil placement. Each capacitor bank to compensate for the leakage inductance was made of five 6.8-nF film capacitors and four 1-nF film capacitors. To convert the high-frequency ac voltage at the receiver side to dc voltage, a rectifier consisting of four SS34 Schottky diodes was used, together with three types of capacitors to further smooth the output voltage: an electrolytic capacitor of 470 μF, a polypropylene capacitor of 1 μF, and two ceramic capacitors of 100 nF. However, due to the manufacturing errors, the coils or compensating capacitors cannot be identical. Therefore, their parameter values were measured by a Keysight E4980AL *LCR* meter at 80 kHz (see Table IV). Since the on-board clock of the FPGA was 40 MHz, each PWM period was configured to cover 500 clock periods, so that an 80-kHz driving frequency was obtained. In this situation, the resolution of the normalized phase shift was $1/250 = 0.004$.

In order to generate experimental data for model identification, we followed the procedure presented in Section V.

1) First, to set up a stationary working point, the stationary inputs were set to $\overline{\Gamma}_1 = 0.7$ and $\overline{\Gamma}_2 = 0.8$, and then, the resulting stationary output was measured to be 7.443 V. At this state, the input power was 7.074 W for the first channel and 5.492 W for the second channel, measured by a Rigol DP832A programmable dc power supply. Given a 9.7-Ω resistive load, the overall efficiency of the prototype was $7.443^2/9.7/(7.074 + 5.472) \cdot 100\% = 45.52\%$. This value was not high, due to the significant misalignment between the transmitter and receiver coils. However, experiments have shown that the efficiency in the SISO case can reach up to 85% under perfect coil alignment.
2) Second, the two inputs were simultaneously perturbed by two uncorrelated PRBS signals in order to persistently excite the system. In particular, $u_1(t)$ was chosen as a PRBS generated from a five-stage shift register at a clock period $50T$, where $T = 0.2$ ms is the sampling interval, while $u_2(t)$ was chosen as a PRBS generated from a six-stage shift register at a clock period $25T$. Both PRBSs had their amplitude switching between ± 0.02. It can be seen that the sampling frequency (5 kHz) is much faster than the bandwidth of the estimated model (58), i.e., 58.6 Hz for the first input channel and 59.65 Hz for the second input channel.
3) Finally, when the test sequences had been applied, the input–output signals were observed at sampling instant $t_k = kT, k = 1, \ldots, 1600$. The sampled input–output data are denoted as $\{y(t_k), u_1(t_k), u_2(t_k)\}_{k=1}^{1600}$; and Fig. 17 shows a portion of input–output observations.

As shown in Fig. 17, the output response does not have any oscillatory component, even if the inputs have numerous sharp changes, suggesting that a first-order model should explain the input–output behavior of the system, according to the guidelines presented in Section IV-A. This initial conjecture was confirmed by estimating first- and second-order models using the experimental data shown in Fig. 17. The estimated first-order model is then

$$x(t) = \frac{-4501}{p + 368.2} u_1(t - 6.72 \cdot 10^{-5}) + \frac{-6644}{p + 374.8} u_2(t - 0.000161) \quad (58)$$

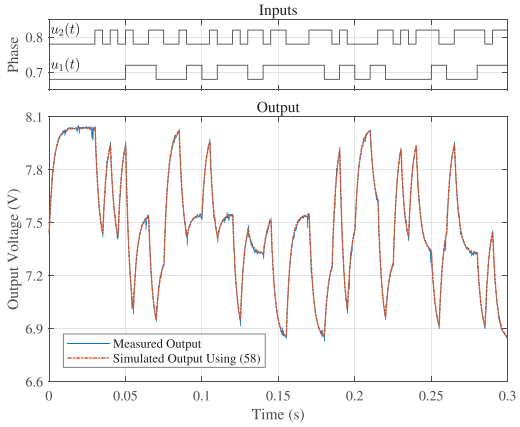

Fig. 17. Portion of experimental data, together with the simulated output using the first-order model (58).

with a fit ratio being 96.49%. Fig. 17 shows a comparison between the measured output and the simulated output of this model. The estimated second-order model is

$$x(t) = \frac{-9.76 \cdot 10^7}{p^2 + 2.21 \cdot 10^4 p + 7.982 \cdot 10^6} u_1(t - 1.48 \cdot 10^{-5}) + \frac{-2.347 \cdot 10^8}{p^2 + 3.576 \cdot 10^4 p + 1.323 \cdot 10^7} u_2(t - 0.000127) \tag{59}$$

with a fit ratio being 96.49%. Comparison of the two fit ratios shows that both models explain the data very well, so that a first-order model is, indeed, sufficient to provide a satisfactory explanation of the experimental data. Note that the noise model was not estimated since, as shown in Fig. 17, the measurement noise level is quite low and so has a negligible impact on the estimated parameters.

Subsequently, 100 independent experiments were carried out to investigate the statistical properties of the parameter estimates. For each experiment, the WPT system was initially in a stationary state, so the initial model state was set to zero in the application of the TFRIVC method. The initial settings were chosen as $n_1 = n_2 = 1$, $m_1 = m_2 = 0$, $\underline{\tau}_1 = \underline{\tau}_2 = 0$ s, $\overline{\tau}_1 = 2.8$ ms, $\overline{\tau}_2 = 2.2$ ms, $\lambda = 100$ rad/s, and $K_1 = K_2 = 5$. The mean values and standard deviations of the resulting parameter estimates generated from the 100 experiments are listed in Table V, showing a very high fit ratio ($\overline{\text{fit}} = 96.1\%$) and a fast convergence rate $\overline{T}_c = 0.27$ s. It is also interesting to observe that the estimated time delays are quite small, only one or two sampling intervals, because the output voltage is sampled directly by CompactRIO. Note that practical WPT systems are seldom in this situation, where sampling of the output voltage is usually done by a remote sensor, with data transferred to the host computer via wireless communication. Inevitably, this introduces longer time delays.

Finally, the responses of the estimated model, as constructed by using the mean parameter values, are given in Table V, when $u_1(t)$ steps from 0 to -0.02 at around the stationary point $\overline{\Gamma}_1 = 0.7$, and when $u_2(t)$ steps from 0 to -0.02 around the stationary point $\overline{\Gamma}_2 = 0.8$. Fig. 18 shows the comparison results, where the step responses of the true system are also plotted. These results confirm again the accuracy and effectiveness of the proposed method.

TABLE V
ESTIMATED FIRST-ORDER MODEL PARAMETERS

Parameter	Value (mean($\pm$std))
$\hat{a}_{1,1}$	366.2($\pm$1.9)
$\hat{b}_{0,1}$	$-4493(\pm 21)$
$\hat{\tau}_1$	$6.691 \cdot 10^{-5}(\pm 9.75 \cdot 10^{-6})$
$\hat{a}_{1,2}$	373($\pm$1.5)
$\hat{b}_{0,2}$	$-6628(\pm 22)$
τ_2	$0.0001673(\pm 3 \cdot 10^{-5})$
$\overline{\text{fit}}$	96.1%($\pm$0.15%)
$\overline{N}_{\text{iter}}$	6
$\overline{T}_c$	0.27 s

$\overline{\text{fit}}$–Mean fit value.
$\overline{N}_{\text{iter}}$–Mean iteration number.
$\overline{T}_c$–Mean computing time.

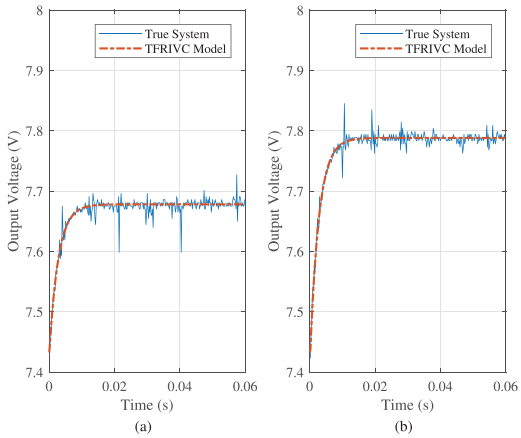

Fig. 18. Responses of the true system and estimated models, when $u_1(t)$ steps from 0 to -0.02 at around the stationary point $\overline{\Gamma}_1 = 0.7$, and when $u_2(t)$ steps from 0 to -0.02 around the stationary point $\overline{\Gamma}_2 = 0.8$. (a) Step response from $u_1(t)$. (b) Step response from $u_2(t)$.

VII. CONCLUSION

In this article, a new method is developed for the data-driven modeling of MISO WPT systems where, in addition to the process parameters, pure time delays and colored measurement noise are estimated simultaneously. In contrast to conventional circuit-theory-based modeling methods that require full information on the circuit, the proposed method is very user-friendly, requiring only sampled input–output data and a few initial settings that can be selected easily according to the suggested guidelines. Most importantly, the proposed method yields simple low-order models plus time delays that are of a form that is well suited for control system design. Simulation results show that the MISO WPT system can be satisfactorily described by a second-order model if the system is underdamped, and that the proposed method generates a very accurate second-order model, even when there is a reasonable level of noise on the sampled data. Experimental results have shown that overdamped systems

can be modeled by a first-order model, and for the prototype used in the real-data experiment, the proposed method yielded a high fit ratio of up to 96% in this first-order modeling scenario.

REFERENCES

[1] A. Kurs, A. Karalis, R. Moffatt, J. D. Joannopoulos, P. Fisher, and M. Soljačić, "Wireless power transfer via strongly coupled magnetic resonances," *Science*, vol. 317, no. 83, pp. 83–86, 2007.

[2] S. Y. R. Hui, W. Zhong, and C. K. Lee, "A critical review of recent progress in mid-range wireless power transfer," *IEEE Trans. Power Electron.*, vol. 29, no. 9, pp. 4500–4511, Sep. 2014.

[3] S. Y. R. Hui and W. W. Ho, "A new generation of universal contactless battery charging platform for portable consumer electronic equipment," *IEEE Trans. Power Electron.*, vol. 20, no. 3, pp. 620–627, May 2005.

[4] B. Kallel, O. Kanoun, and H. Trabelsi, "Large air gap misalignment tolerable multi-coil inductive power transfer for wireless sensors," *IET Power Electron.*, vol. 9, no. 8, pp. 1768–1774, Jun. 2016.

[5] P. Si, A. P. Hu, S. Malpas, and D. Budgett, "A frequency control method for regulating wireless power to implantable devices," *IEEE Trans. Biomed. Circuits Syst.*, vol. 2, no. 1, pp. 22–29, Mar. 2008.

[6] H. Liu, Q. Shao, and X. Fang, "Modeling and optimization of class-E amplifier at subnominal condition in a wireless power transfer system for biomedical implants," *IEEE Trans. Biomed. Circuits Syst.*, vol. 11, no. 1, pp. 35–43, Feb. 2017.

[7] G. A. Covic, J. T. Boys, M. L. Kissin, and H. G. Lu, "A three-phase inductive power transfer system for roadway-powered vehicles," *IEEE Trans. Ind. Electron.*, vol. 54, no. 6, pp. 3370–3378, Dec. 2007.

[8] F. Musavi and W. Eberle, "Overview of wireless power transfer technologies for electric vehicle battery charging," *IET Power Electron.*, vol. 7, no. 1, pp. 60–66, Jan. 2014.

[9] X. Dai, J. C. Jiang, and J. Q. Wu, "Charging area determining and power enhancement method for multiexcitation unit configuration of wirelessly dynamic charging EV system," *IEEE Trans. Ind. Electron.*, vol. 66, no. 5, pp. 4086–4096, May 2019.

[10] I. J. Yoon and H. Ling, "Investigation of near-field wireless power transfer under multiple transmitters," *IEEE Antennas Wireless Propag. Lett.*, vol. 10, pp. 662–665, 2011.

[11] D. Ahn and S. Hong, "Effect of coupling between multiple transmitters or multiple receivers on wireless power transfer," *IEEE Trans. Ind. Electron.*, vol. 60, no. 7, pp. 2602–2613, Jul. 2013.

[12] R. Johari, J. V. Krogmeier, and D. J. Love, "Analysis and practical considerations in implementing multiple transmitters for wireless power transfer via coupled magnetic resonance," *IEEE Trans. Ind. Electron.*, vol. 61, no. 4, pp. 1774–1783, Apr. 2014.

[13] H. D. Lang and C. D. Sarris, "Semidefinite relaxation-based optimization of multiple-input wireless power transfer systems," *IEEE Trans. Microw. Theory Techn.*, vol. 65, no. 11, pp. 4294–4306, Nov. 2017.

[14] Y. Li, R. Mai, L. Lu, T. Lin, Y. Liu, and Z. He, "Analysis and transmitter currents decomposition based control for multiple overlapped transmitters based WPT systems considering cross couplings," *IEEE Trans. Power Electron.*, vol. 33, no. 2, pp. 1829–1842, Feb. 2018.

[15] S. Huh and D. Ahn, "Two-transmitter wireless power transfer with optimal activation and current selection of transmitters," *IEEE Trans. Power Electron.*, vol. 33, no. 6, pp. 4957–4967, Jun. 2018.

[16] D. Czarkowski and M. K. Kazimierczuk, "Energy-conservation approach to modeling PWM DC-DC converters," *IEEE Trans. Aerosp. Electron. Syst.*, vol. AES-29, no. 3, pp. 1059–1063, Jul. 1993.

[17] S. Zheng and D. Czarkowski, "Modeling and digital control of a phase-controlled series–parallel resonant converter," *IEEE Trans. Ind. Electron.*, vol. 54, no. 2, pp. 707–715, Apr. 2007.

[18] Z. U. Zahid *et al.*, "Modeling and control of series–series compensated inductive power transfer system," *IEEE J. Emerg. Sel. Topics Power Electron.*, vol. 3, no. 1, pp. 111–123, Mar. 2015.

[19] H. Hao, G. A. Covic, and J. T. Boys, "An approximate dynamic model of LCL-T-based inductive power transfer power supplies," *IEEE Trans. Power Electron.*, vol. 29, no. 10, pp. 5554–5567, Oct. 2014.

[20] S. Li and C. T. Mi, "Wireless power transfer for electric vehicle applications," *IEEE J. Emerg. Sel. Topics Power Electron.*, vol. 3, no. 1, pp. 4–17, Mar. 2015.

[21] A. Ayachit and M. K. Kazimierczuk, "Transfer functions of a transformer at different values of coupling coefficient," *IET Circuits, Devices Syst.*, vol. 10, no. 4, pp. 337–348, Jul. 2016.

[22] J. Tang, S. Dong, C. Cui, and Q. Zhang, "Sampled-data modeling for wireless power transfer systems," *IEEE Trans. Power Electron.*, vol. 35, no. 3, pp. 3173–3182, Mar. 2020.

[23] S. Samanta and A. K. Rathore, "Small-signal modeling and closed-loop control of a parallel–series/series resonant converter for wireless inductive power transfer," *IEEE Trans. Ind. Electron.*, vol. 66, no. 1, pp. 172–182, Jan. 2019.

[24] Q. Deng *et al.*, "Modeling and control of inductive power transfer system supplied by multiphase phase-controlled inverter," *IEEE Trans. Power Electron.*, vol. 34, no. 9, pp. 9303–9315, Sep. 2019.

[25] F. Chen, H. Garnier, Q. Deng, M. K. Kazimierczuk, and X. Zhuan, "Control-oriented modeling of wireless power transfer systems with phase-shift control," *IEEE Trans. Power Electron.*, vol. 35, no. 2, pp. 2119–2134, Feb. 2020.

[26] L. Ljung, *System Identification—Theory for the User*. Upper Saddle River, NJ, USA: Prentice-Hall, 1999.

[27] H. Garnier and L. Wang (Eds.), *Identification of Continuous-Time Models From Sampled Data*. London, U.K.: Springer-Verlag, 2008.

[28] P. C. Young, *Recursive Estimation and Time-Series Analysis: An Introduction for the Student and Practitioner*. Berlin, Germany: Springer-Verlag, 2011.

[29] T. T. Vu, S. O'Driscoll, and J. V. Ringwood, "Nonlinear dynamic transformer time-domain identification for power converter applications," *IEEE Trans. Power Electron.*, vol. 29, no. 1, pp. 318–327, Jan. 2014.

[30] V. Valdivia, A. Barrado, A. Lázaro, P. Zumel, C. Raga, and C. Fernández, "Simple modeling and identification procedures for "black-box" behavioral modeling of power converters based on transient response analysis," *IEEE Trans. Power Electron.*, vol. 24, no. 12, pp. 2776–2790, Dec. 2009.

[31] M. Ahmeid, M. Armstrong, S. Gadoue, M. Al-Greer, and P. Missailidis, "Real-time parameter estimation of DC–DC converters using a self-tuned kalman filter," *IEEE Trans. Power Electron.*, vol. 32, no. 7, pp. 5666–5674, Jul. 2017.

[32] M. Al-Greer, M. Armstrong, M. Ahmeid, and D. Giaouris, "Advances on system identification techniques for DC–DC switch mode power converter applications," *IEEE Trans. Power Electron.*, vol. 34, no. 7, pp. 6973–6990, Jul. 2019.

[33] F. Chen, X. Zhuan, H. Garnier, and M. Gilson, "Issues in separable identification of continuous-time models with time-delay," *Automatica*, vol. 94, pp. 258–273, 2018.

[34] A. Ayachit, F. Corti, A. Reatti, and M. K. Kazimierczuk, "Zero-voltage switching operation of transformer class-E inverter at any coupling coefficient," *IEEE Trans. Ind. Electron.*, vol. 66, no. 3, pp. 1809–1819, Mar. 2019.

[35] M. K. Kazimierczuk and D. Czarkowski, *Resonant Power Converters*. New York, NY, USA: IEEE Press and Wiley, 2011.

[36] P. C. Young, "Data-based mechanistic modelling, generalised sensitivity and dominant mode analysis," *Comput. Phys. Commun.*, vol. 117, pp. 113–129, 1999.

[37] M. Bojarski, E. Asa, K. Colak, and D. Czarkowski, "Analysis and control of multiphase inductively coupled resonant converter for wireless electric vehicle charger applications," *IEEE Trans. Transp. Electrific.*, vol. 3, no. 2, pp. 312–320, Jun. 2017.

[38] M. K. Kazimierczuk, "Synthesis of phase-modulated resonant DC/AC inverters and DC/DC convertors," *Proc. Inst. Elect. Eng. B—Electr. Power Appl.*, vol. 139, no. 4, pp. 387–394, Jul. 1992.

[39] D. Czarkowski and M. K. Kazimierczuk, "Phase-controlled CLL resonant converter," in *Proc. IEEE Appl. Power Electron. Conf.*, San Diego, CA, USA, Mar. 7–11 1993, pp. 432–438.

[40] N. Kollipara, M. K. Kazimierczuk, A. Reatti, and F. Corti, "Phase-control and power optimization of LLC converter," in *Proc. IEEE Int. Symp. Circuits Syst.*, Sapporo, Japan, May 26–29 2019, pp. 1–5.

[41] P. C. Young, H. Garnier, and M. Gilson, "Refined instrumental variable identification of continuous-time hybrid Box–Jenkins models," in *Identification Continuous-Time Models From Sampled Data*, H. Garnier and L. Wang Eds. London, U.K.: Springer-Verlag, 2008, pp. 91–132.

[42] P. C. Young, "Refined instrumental variable estimation: Maximum likelihood optimization of a unified Box–Jenkins model," *Automatica*, vol. 51, no. 1, pp. 35–46, 2015.

[43] P. C. Young and H. Garnier, "Identification and estimation of continuous-time data-based mechanistic (DBM) models for environmental systems," *Environ. Model. Softw.*, vol. 21, no. 8, pp. 1055–1072, 2006.

[44] H. Garnier and P. C. Young, "The advantages of directly identifying continuous-time transfer function models in practical applications," *Int. J. Control*, vol. 87, no. 7, pp. 1319–1338, 2014.

[45] H. Garnier, "Direct continuous-time approaches to system identification. Overview and benefits for practical applications," *Eur. J. Control*, vol. 24, pp. 50–62, 2015.
[46] H. Garnier, M. Gilson, P. C. Young, and E. Huselstein, "An optimal IV technique for identifying continuous-time transfer function model of multiple input systems," *Control Eng. Pract.*, vol. 15, no. 4, pp. 471–486, 2007.
[47] A. J. Jakeman, L. P. Steele, and P. C. Young, "Instrumental variable algorithms for multiple input systems described by multiple transfer functions," *IEEE Trans. Syst., Man, Cybern.*, vol. SMC-10, no. 10, pp. 593–602, Oct. 1980.
[48] F. Chen, H. Garnier, and M. Gilson, "Robust identification of continuous-time models with arbitrary time-delay from irregularly sampled data," *J. Process Control*, vol. 25, pp. 19–27, 2015.

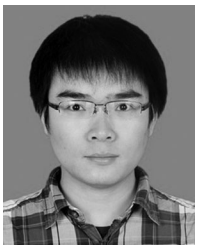

Fengwei Chen was born in Chongqing, China. He received the B.Eng. degree in automation and the M.Eng. degree in control theory and control engineering from Wuhan University, Wuhan, China, in 2009 and 2011, respectively, and the Ph.D. degree in automatic control from the Université de Lorraine, Nancy, France, in 2014.

From 2015 to 2016, he was a Lecturer with the Dalian University of Technology, Dalian, China. Since 2017, he has been with Wuhan University, where he is currently an Associate Researcher. His research interests include system identification and parameter estimation, with applications to wireless power transfer.

Peter C. Young received the B.Tech. and M.Sc. degrees in aeronautical engineering from Loughborough University, U.K., in 1962 and 1965, respectively, and the M.A. and Ph.D. degrees in automatic control and systems engineering from the University of Cambridge, U.K.

From 1968 to 1970, he carried out research on self-adaptive control for the US Navy in California. In 1970, he was appointed as a Lecturer in the Engineering Department and fellow of Clare Hall, University of Cambridge. From 1975 to 1981, he was a Research Professor at the Australian National University in Canberra, Australia, where he helped to establish the Centre for Resource and Environmental Studies. From 1981 to 1987, he was the Head of the Environmental Science Department at Lancaster University, where he was instrumental in establishing the Institute of Environmental and Biological Sciences, and is currently an Emeritus Professor of Environmental Systems. In 1992, he helped to set up the Lancaster Centre for Forecasting with Prof. Robert Fildes and then directed the Centre for Research on Environmental Systems and Statistics at Lancaster. He has published over 300 papers and chapters in books; and authored or coauthored several books, including *Recursive Estimation and Time Series Analysis* (2011) and *True Digital Control* (2013). He has also been instrumental, over many years, in the development of CAPTAIN, a noncommercial MATLAB toolbox for the recursive estimation, forecasting and control of discrete and continuous-time dynamic systems. He continues to pursue research on these topics, with applications in diverse areas of research and development.

Hugues Garnier received the M.S. degree in control engineering and signal processing and the Ph.D. degree in automatic control from Université Henri Poincaré, Nancy 1, France, in 1993 and 1995, respectively.

He has been a Professor of control theory and applications with the University of Lorraine, Nancy, France, since 2003. He was a Visiting Researcher with the University of Newcastle, Australia, from 2002 to 2003, and with the University of California, San Diego, CA, USA, from 2012 to 2013. Since 2000, he has been very active in promoting direct continuous-time model-based approaches to system identification. He was the Editor of two books and was the Guest Editor for three special issues of international journals. He is also behind CONTSID, a noncommercial MATLAB toolbox for continuous-time system identification. His main research interests include system identification. His current applications include problems such as data-based modeling for battery management systems, satellite attitude control, or large flexible space structure control.

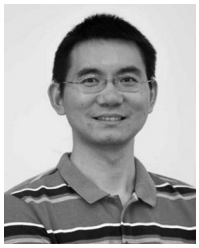

Qijun Deng received the B.S. and M.Sc. degrees in mechanical engineering and the Ph.D. degree in computer application technology from Wuhan University, Wuhan, China, in 1999, 2002, and 2005, respectively.

In June 2005, he joined with the Department of Automation (which is now merged into the School of Electrical Engineering and Automation), Wuhan University, where he is currently a Professor. From 2013 to 2014, he was a Visiting Scholar with the New York University Tandon School of Engineering, New York, NY, USA. His research interests include wireless power transfer, distribution automation, and electrical power informatics.

Marian K. Kazimierczuk (Fellow, IEEE) received the M.S., Ph.D., and D.Sc. degrees in electronics engineering from the Department of Electronics, Warsaw University of Technology, Warsaw, Poland, in 1971, 1978, and 1984, respectively.

From 1972 to 1978, he was a Teaching and Research Assistant with the Department of Electronics, Institute of Radio Electronics, Warsaw University of Technology, where he was an Assistant Professor from 1978 to 1984. In 1984, he was a Project Engineer with Design Automation Inc., Lexington, MA, USA. From 1984 to 1985, he was a Visiting Professor with the Department of Electrical and Computer Engineering, Virginia Polytechnic Institute and State University, Blacksburg, VA, USA. Since 1985, he has been with the Department of Electrical Engineering, Wright State University, Dayton, OH, USA, where he is currently a University Distinguished Professor. He has authored or coauthored 210 peer-reviewed journal papers and 260 conference papers and holds eight patents. He is also the author/co-author of seven books entitled *Electronic Devices: A Design Approach* (Englewood Cliffs, NJ, USA: Prentice-Hall/Pearson, 2004), *Laboratory Manual for Electronic Devices: A Design Approach* (Englewood Cliffs, NJ, USA: Prentice-Hall/Pearson, 2004), *Resonant Power Converters* (2nd ed. Hoboken, NJ, USA: Wiley, 2011), *Pulse-Width Modulated DC-DC Power Converters* (2nd ed. Hoboken, NJ, USA: Wiley, 2016), *Laboratory Manual for Pulse-Width Modulated DC-DC Power Converters* (Hoboken, NJ, USA: Wiley, 2016), *High-Frequency Magnetic Components* (2nd ed. Hoboken, NJ, USA: Wiley, 2014), and *RF Power Amplifiers* (2nd ed. Hoboken, NJ, USA: Wiley, 2015). His research interests include high-frequency high-efficiency switching-mode tuned power amplifiers, resonant and pulsewidth modulated dc–dc power converters, dc–ac inverters, high-frequency soft-switching rectifiers, electronic ballasts, modeling and control of converters, new converter topologies, gate drivers, high-frequency magnetics, wireless power transfer, renewable energy sources, power factor correction, and wide-bandgap power semiconductor devices.

Dr. Kazimierczuk was the recipient of the Best Paper Award from *IET Power Electronics* in 2012. He has received Presidential Research, Teaching, and Service Awards as well as the Trustee's Award from Wright State University. He was an Associate Editor for the IEEE TRANSACTIONS ON CIRCUITS AND SYSTEMS and the *Journal of Circuits, Systems, and Computers*. He is an Associate Editor for the IEEE TRANSACTIONS ON INDUSTRIAL ELECTRONICS, the *International Journal of Circuits Theory and Applications*, and *IET Circuits, Devices, and Systems*.